



Italian Chapter of the
European Society of Biomechanics
(ESB-ITA)

ESB-ITA 2012 Meeting

In conjunction with the Italian National
Bioengineering Group (GNB) Congress 2012

Università degli Studi Roma Tre, Roma – June 29, 2012
Organizing Committee: L Cristofolini, F Di Puccio, G Dubini, F Taddei

Book of Abstracts



Programma ESB-ITA2012

Aula Magna

Lecture magistrali congiunte ESB-ITA 2012 – GNB2012

11:30

Moderatore Prof. Roberto Contro

Prof. Aurelio Cappozzo

*Dipartimento di Scienze del Movimento Umano e dello Sport,
Università degli Studi di Roma "Foro Italico", Roma*

De Motu Animalium: from Borelli to the foundation of the Italian Chapter of the
European Society of Biomechanics and beyond

Prof. Oussama Khatib

Artificial Intelligence Laboratory, Computer Science Department, Stanford University

Robots and the human

11:30 – 12:45

13:15

Pranzo

14:00

Inizio Meeting ESB-ITA2012, benvenuto

Presentazioni orali

14:15

Moderatori: Francesco Migliavacca - Valentina Camomilla

Gallo Diego

Department of Mechanical and Aerospace Engineering, Politecnico di Torino (Italy)

Helical flow in carotid bifurcation: influence on exposure to disturbed shear

Celi Simona

Institute of Clinical Physiology, CNR, Heart Hospital, Massa, Italia

FE simulations on the effect of regional variations of material properties and wall
thickness on AAA

una presentazione ogni 12 min

Conti Michele

Dipartimento di Meccanica Strutturale, Università di Pavia

Finite Element Analysis of Carotid Artery Stenting: from diagnosis to prediction

Dall'Ara Enrico

Inst. Lightweight Design and Structural Biomechanics, Vienna Univ. of Technology

Non-Linear QCT-based FE models predict in vitro femoral strength better than DXA

Falcinelli Cristina

Laboratorio di Bioingegneria Computazionale, Istituto Ortopedico Rizzoli, Italy

FE-based strength estimation for the prediction of femoral neck fracture

Mattei Lorenza

Dept of Mechanical, Nuclear and Production Engineering, University of Pisa

Analytical wear model of hip implants

Nava Michele

LaBS, Department of Structural Engineering, Politecnico di Milano, Milano, Italy

Two-photon polymerization for engineering stem cell niches

Massai Diana

Politecnico di Torino, Italy

Innovative low-cost microgravity bioreactor for hydrogel-based regenerative medicine strategies

Riva federico

Dept Electronics, Computer Sciences and Systems, University of Bologna, Italy

Orbital stability analysis of gait: model and experimental analysis comparison

Spatafora Grazia

LaBS, Dipartimento di Ingegneria Strutturale, Politecnico di Milano

Mechanical properties of native and engineered cartilage from indentation tests

Poster

Moderatore: Alberto Audenino

16:15 – 17:00

Abouhossein Alireza

Dep of Electrical Computer Science and System Engineering, University of Bologna

Dynamic Responses of a 3-Dimensional Multibody Model of a Biofidelic Surrogate Neck and Head Under Compressive Follower Load and Variability of Impact Velocity and Angle of impact During Head-First Impact

Bianchi Elena

LaBS, Department of Structural Engineering - Politecnico di Milano

Study of drug delivery dynamics in pediatric central venous infusion systems

Bianchi Elena

LaBS, Department of Structural Engineering - Politecnico di Milano

Buoyancy driven flows in a microfluidic device for PCR applications

Carniel Emanuele Luigi

Dept. of Industrial Engineering, Centre of Mechanics of Biological Materials, University of Padova,

Constitutive models for the investigation of biomechanical functionality of colon region

Celi Simona

Institute of Clinical Physiology, CNR, Heart Hospital, Massa, Italia

Design and characterization of a non-homogeneous elastosonographic breast phantom using PVA-C

Celi Simona

Institute of Clinical Physiology, CNR, Heart Hospital, Massa, Italia

FE simulations of 3D atherosclerotic vessels by means of OCT images

Manini Simone

Biomedical Engineering Department, Mario Negri Institute, Bergamo

Patient specific multi-scale hemodynamic computational model for planning vascular access surgery in hemodialysis patients

Tersi Luca

Health Sciences and Technologies Interdept Center for Industrial Research Bologna

Effects of calibration errors on 3D kinematics quantification with fluoroscopy

Volandri Gaia

Dept. Mechanical, Nuclear and Production Engineering, University of Pisa

Development and sensitivity study of a hybrid FE-MB model of the human middle ear

17:00

Premiazioni (presentazione, poster, logo)

17:15

Assemblea Capitolo Italiano della *European Society of Biomechanics*

18:00

Conclusione Meeting

Lista dei Contributi

- Abouhossein *et al.* Dynamic Responses of a 3D multibody model of a biofidelic surrogate shoulder neck head under compressive follower load and variability of impact velocity and angle of impact during head-first impact
- Bianchi *et al.* Study of drug delivery dynamics in pediatric central venous infusion systems
- Bianchi *et al.* Buoyancy driven flows in a microfluidic device for PCR applications
- Carniel *et al.* Constitutive models for the investigation of biomechanical functionality of colon region
- Celi *et al.* Design and characterization of a non-homogeneous elastosonographic breast phantom using PVA-C
- Celi *et al.* FE simulations on the effects of regional variations of material properties and wall thickness on AAA
- Conti *et al.* Finite Element Analysis of Carotid Artery Stenting: from diagnosis to prediction
- Dall'Ara *et al.* Non-Linear QCT-based FE models predict in vitro femoral strength better than DXA
- Falcinelli *et al.* FE-based strength estimation for the prediction of femoral neck fracture
- Gallo *et al.* Helical flow in carotid bifurcation: influence on exposure to disturbed shear
- Manini *et al.* Patient specific multi scale hemodynamic computational model for planning vascular access surgery in hemodialysis patients
- Massai *et al.* Innovative low-cost microgravity bioreactor for hydrogel-based regenerative medicine strategies
- Mattei *et al.* Analytical wear model of hip implants
- Nava *et al.* Two-photon polymerization for engineering stem cell niches
- Riva *et al.* Orbital stability analysis of gait: model and experimental analysis comparison
- Spatafora *et al.* Mechanical properties of native and engineered cartilage from indentation tests
- Tersi *et al.* Effects of calibration errors on 3D kinematics quantification with fluoroscopy
- Volandri *et al.* Development and sensitivity study of a hybrid FE-MB model of the human middle ear

Dynamic Responses of a 3-Dimensional Multibody Model of a Biofidelic Surrogate Neck and Head Under Compressive Follower Load and Variability of Impact Velocity and Angle of impact During Head-First Impact

Alireza Abouhossein¹, Christopher R. Dennison², Daniel Dressler² and Peter A. Cripton²

¹*Department of Electrical Computer Science and System Engineering, University of Bologna, Center for research on Complex Automated Systems (CASYS), Via Pepoli 3/2, Bologna, Italy, alireza.abouhossein@unibo.it*

²*Orthopaedic and Injury Biomechanics Group, Department of Mechanical Engineering University of British Columbia, and The International Collaboration on Repair Discoveries (ICORD), Vancouver, British Columbia, Canada*

Abstract—The neck and spinal cord injuries associated with both traffic and sports accidents have tremendous socioeconomic effects on human quality of life. Validated computational models capable of predicting the neck response under impact loads are invaluable tools to evaluate strategies and preventive measures for head-first impact. A three-dimensional multi-body dynamics model of an existing experimental surrogate neck is developed to simulate head-first impacts and to understand both kinematics and kinetics responses of the neck during different velocity and +15 degrees contact. The model is validated for resultant head and neck against the experimental set-up. The resultant head and neck loads are substantially increased in the simulation with higher velocities. At 5 m/s impact velocity both first order and second order buckling modes were observed.

Keywords—Dynamic modeling, Neck injury, Cervical spine, Multi-body modelling.

I. INTRODUCTION

UNDERSTANDING the mechanism of the neck injuries is important due to its significant effects on human quality of life. Injuries occurring to the head and neck due to vehicle or sports head-on collisions may have long lasting effect on function of human in his/her daily activities. Injuries to the neck are specifically considered life threatening since it may affect the phrenic nerve that is responsible for balancing pressure in the human diaphragm. Any sudden damages to the phrenic nerve may affect human breath mechanism and may lead full or partial disability or even death. The exact mechanism of cervical spine and spinal cord injury due to head-first impact is still unknown. However, studies have shown that the neck compression as a result of the head sudden stop and continuous movement of the torso while neck hyper-flexion and hyper-extension occurs due to combination of the bending moment and compression loads are clearly considered some of the main causes of neck injuries [1]. Three main preventive strategies have been suggested for reducing injuries to the neck during axial impact are, 1)

friction reduction from the surface impact to allow the head to escape the stopping surface and 2) specialized brace such as the Leatt Brace which constrains the head to prevent hyper flexion/extension or side bending or 3) Pro-Neck-TorTM that provides an escape path for the head by its inner-shell movement. To be able to continue to introduce new strategies and preventive tools for any type of neck injuries requires well understanding of biomechanical responses of the neck and head under the different environmental conditions and the human soft tissues variability. Previous studies have shown variations in cervical joint stiffness, damping, mass and inertia have influenced the compression loads of the neck resulting in buckling of the neck. Computer models and specifically multi-body modelling approach have been the promising tools to provide insight into injury mechanism associated with inertia. In addition, computer models developed in biomechanics domain reduce costs associated with expensive cadaveric tests, accommodating possible sensitivity analysis that are costly and time consuming otherwise. Computer models also provide an effective means to evaluate preventive tools and strategies. Hence, the purpose of the current study was to develop a three-dimensional multi-body dynamics model of an existing experimental surrogate neck to simulate head-first impacts [2] and specifically, to evaluate the influence of the impact velocity and angle of impact on the biomechanical response of the neck.

II. METHODS

A three-dimensional articulating multibody model of head and neck was developed using MD ADAMS 2011 dynamic software (Version 2011, Santa Ana, USA). The vertebrae (C1-C7) and T1 were imported to the software as geometrical entities representing the physical model with corresponding inertia, masses and center of CoG. The head was digitized from a Hybrid III 50th percentile anthropometric dummy.

Proper linear translational and non-linear rotational stiffness [3] were assigned at the assumed center of rotation between every superior/inferior vertebrae. Contact interaction was defined between every vertebra to resemble the proper structural integrity of the physical model. The follower load was accommodated so the compression was exerted along the center of rotation of each vertebra minimizing bending moment and shear force. A validation simulation was conducted against the experimental work by Nelson and Cripton (2010). The validation was performed for an impact velocity of 3 m/s with a follower load of 104 N and for pure vertical impact [2]. The multi-body model was further run for impact velocities of 3, and 5 m/s for both scenarios with and without compressive follower load and plus 15 degree angle between head and surface impact. The simulation kinetics and kinematics results were recorded for analysis.

III. RESULTS

The neck and head resultant forces of the simulation for 3 m/s with a compressive follower load are comparable to the Nelson and Cripton (2010) experimental reported loading scenarios. Figure 1 depicts that the peak resultant head and lower neck forces for 3 m/s impact velocity with 104 N follower load were measured to be 27.4 kN and 3.9 kN, respectively.

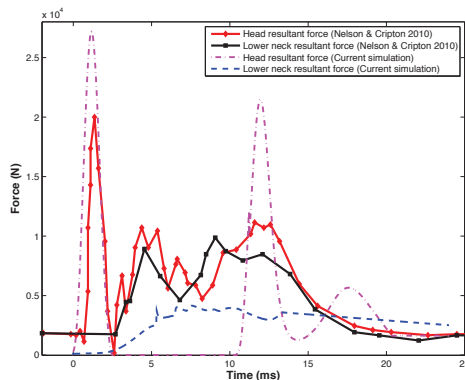


Fig. 1. kinetics validation The plot of simulation are shown against the experimental tests for 3 m/s head-first impact at pure vertical contact

The large resultant head load is due to the rigid definition contact between head and the impact surface. These results lie between reported corridors by [2] and [1]. A delay of 2.5 to 3 ms was observed between onset of resultant head impact load and lower neck force response in the simulation. This delay matches the delay reported by [2]. The peak neck and head forces were measured to be of a higher magnitude for the models with higher velocities in both with (*i.e.* 3.9 kN for 3 m/s vs 8.1 kN for 5 m/s) and without follower load (*i.e.* 3.5 kN for 3 m/s vs 7.2 kN for 5 m/s). The resultant head loads was measured to be lower during the impact with a rigid surface having an angles of +15 degree from the horizontal line of contact. This is contrary to the lower neck resultant force measured during the latter simulation showing a slight increase without follower load (*i.e.* 3.7 kN for 3 m/s). However

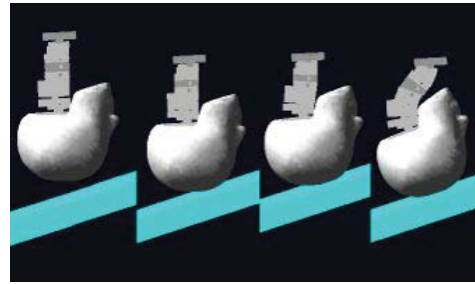


Fig. 2. Second-order buckling in the dynamically loaded head and neck simulation was observed for both with and without follower load and at zero and +15 degree contact for 5 m/s impact velocity. Here, for the representation purposes the photos are shown for the +15 degree head and impact contact. From Left to Right: 1) Before impact, 2) 10 ms after impact, 3) 17 ms after impact 4) 22 ms after impact

the neck load measured to be almost unchanged for contact angles of +15 degree with a follower load (*i.e.* 3.9 kN for 3 m/s).

No major buckling was registered for the 3 m/s velocity impact for both zero and +15 degree angle of head and surface contact with and without the follower load. However, both the first order buckling and the second order buckling modes were observed for 5 m/s impact velocities at both zero and +15 degrees impact angle and with and without follower loads consideration (Figure 2).

IV. DISCUSSION

There are a few limitation with the current multi-body model. The head in the ADAMS model has rigid properties resulting in less deformation and energy absorption than likely occurs in vivo. Therefore, a larger load magnitude closer to the upper part of the validation corridor from [1] was observed for the head impact loads. The visco-elastic values of the discs are load-history dependent, here a linear damping are assigned to every IVD to attenuate the low frequency noise during the impact simulation. The simulation study indicates that the compressive follower load and the initial velocity of the impact influence the neck peak compression forces. It also showed that the higher order buckling modes were recorded during higher impact loads and larger impact angles. At 5 m/s impact velocity both first order and second order buckling were observed in the simulation model. This may be explained by the fact that a dynamic equilibrium transforms from one level configuration to another at higher compressive loads.

REFERENCES

- [1] R. W. Nightingale, J. H. McElhaney, W. J. Richardson, and B. S. Myers, (1996), *Dynamic responses of the head and cervical spine to axial impact loading*, Journal of biomechanics, vol. 29, no. 3, pp. 307318.
- [2] T. S. Nelson and P. A. Cripton, (2010), *A New Biofidelic Sagittal Plane Surrogate Neck for Head-First Impacts*, Traffic Injury Prevention, vol. 11, no. 3, pp. 309319.
- [3] J. A. Wheeldon, F. A. Pintar, S. Knowles, and N. Yoganandan, (2006), *Experimental flexion/extension data corridors for validation of finite element models of the young, normal cervical spine*, Journal of biomechanics, vol. 39, no. 2, pp. 375380.

Study of drug delivery dynamics in pediatric central venous infusion systems

E. Bianchi¹, F. Nason^{1,2}, V. Thurner¹, G. Pennati¹

¹ Laboratory of Biological Structure Mechanics, Department of Structural Engineering - Politecnico di Milano (MI) Italy

² Bioengineering Department, Politecnico di Milano (MI) Italy

Abstract—Central venous catheters (CVCs) are extensively used in the operating room and intensive care unit for continuous infusion of drugs driven by pumps. Precise control of drug delivery is crucial for patient safety and proper treatment: as these infusions are highly concentrated, any sudden variation or lag in the delivery of these drugs can be significant. A common drug infusion system in use in a paediatric unit has been analysed to verify the occurrence of delays in the drug administration. The detected anomalies were attributed to an unexpected fluid dynamic behaviour of the main connector of the system. The four parallel port connector for multiple low-flow intravenous infusions was investigated by CFD simulation, focusing on the flow field and on the drug kinetics inside the tubing system.

Keywords—drug delivery system, continuous infusion, paediatrics, four parallel port connector.

I. INTRODUCTION

CENTRAL venous catheters (CVCs) are extensively used in the operating room and intensive care unit for continuous infusion of vasoactive, inotropic, antidysrhythmic, sedative, and analgesic drugs driven by pumps. Precise control of drug delivery is crucial for patient safety and proper treatment: as these infusions are highly concentrated, any sudden variation or lag in the delivery of these drugs can be significant [1]. Stopcocks are ubiquitously used to deliver multiple drug infusions. Devices designed for adults are often used in the treatment of pediatric patients, which commonly require multiple, very low flow rate drips containing specific drugs [2]. A number of studies [3, 4] were carried out to investigate drug delivery kinetics in a pediatric central venous infusion systems. Previous works focusing on CVCs commonly used in clinical settings demonstrated that syringe size, drug flow rate and connection tubing impact on the onset of an infusion [3]. Considerable attention has been directed towards optimizing pump design to reduce likelihood of clinically significant fluctuations in drug delivery, while less attention has been paid to other components of infusion system [5].

The aim of this study is to investigate drug delivery through commonly used pediatric infusion systems at flow rates representative of those encountered in pediatric intensive care unit. This work was carried out in collaboration with the neonatal unit of the A. Manzoni Hospital in Lecco, where doctors reported a significant delay in the effect of drug administration with respect to the expected time, mainly occurring if the rate of drug is negligible compared the carrier rate. The expected time was estimated [5] as:

$$\tau = \frac{V}{Q_D + Q_C} \quad (1)$$

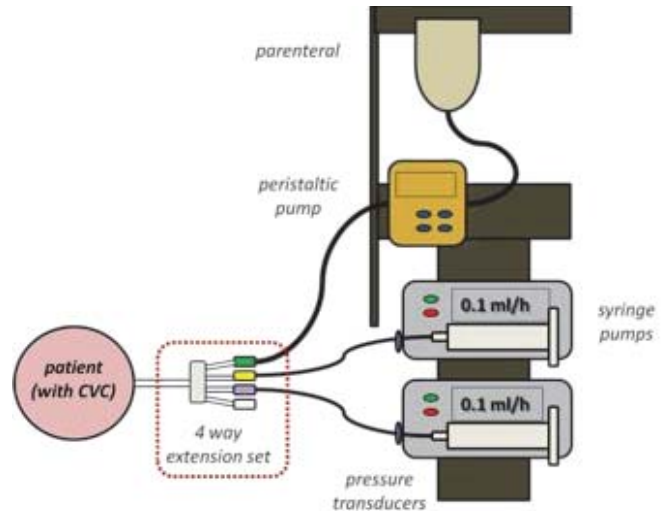


Fig. 1. Sketch of the infusion system, composed by: a parenteral solution delivered to the patient through a peristaltic pump; syringe pumps for drug delivery; a four parallel ports connector and a CVC inserted in the patient.

where V is the priming volume, Q_D is the drug rate and Q_C is the parenteral flow rate. We analyzed in depth the system currently in use (Fig. 1), which is composed by: a parenteral solution delivered to the patient through a peristaltic pump (Asena GW, Alaris medical systems); syringe pumps (Asena CC, Alaris medical systems) for drug delivery; a four parallel port connector (MFX2243E, Alaris medical systems) and a CVC inserted in the patient. A first study focused on the effect of the compliance of the tubing, geometry and dimensions of the syringes adopted and performances of the syringe pump, even in the case of displacing the pump during injection. It was demonstrated that none of these aspects significantly affect the infusion dynamics. This study, therefore focuses on drug kinetics inside the tubing system (Fig. 1 - red box), with particular attention to the four parallel port connector for multiple low-flow intravenous infusions.

II. MATERIALS AND METHODS

CAD models of both tubing and four-port connector and their meshes were generated by means of the solid modeller ICEM (Ansys Inc., Canonsburg, PA, USA). The finite volume code Fluent (Ansys Inc., Canonsburg, PA, USA) was used to address the problem. The computational domain was split in three different sub-domains, as shown in Fig. 2. The first domain is composed by the inlet tubes delivering drugs and parenteral solution; the second one comprises the four parallel port connector, while the third one is the catheter that is inserted in the patient's umbilical vein.

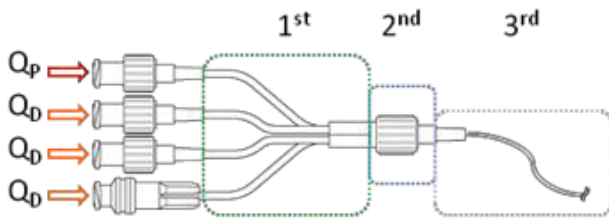


Fig. 2. Sketch of the three computational sub-domains.

As far as the first domain, the four inlets were modelled separately. For each tube, an axisymmetric mesh with $4 \cdot 10^4$ quadrilateral elements was built. The second sub-domain was meshed with $4 \cdot 10^6$ hexahedral elements; thanks to the symmetry of the geometry just half domain was considered. Finally, for the third part of the domain, as for the second part, half domain was simulated, and a mesh of $8 \cdot 10^6$ hexahedral elements was obtained. A sensitivity analysis was carried out to assess the independency on the solution of the grid. In particular, we simulated the case of one inlet perfused with the carrier solution and another one with dopamine. In the fluid-dynamic analyses, the steady-state Navier–Stokes equations for incompressible fluids were solved. Flat velocity profiles were applied at the two inlets in the first sub-domain. Mean flow rates of 10 ml/h and 0.1 ml/h were applied to the parenteral and the drug inlets respectively. For the second and the third sub-domains velocity parabolic profile were imposed at two of the four port connector inlets and at the catheter inlet respectively. Zero pressure was imposed at the outlet. No-slip conditions were applied to the walls. Transient advection-diffusion analyses were subsequently solved with an uncoupled approach. Uniform drug concentrations of 0 and 1 were imposed at the inlets in the first sub-domain corresponding to parenteral solution and drug respectively. Concentration profiles at the outlets were then extracted and adopted as inlet boundary conditions for the four port connector, through a specifically implemented user defined function. Finally, concentration profiles at the outlet of the four-port connector were given as inlet boundary conditions for the catheter. Zero diffusive flux was applied at the outlet. Drug diffusivity in the parenteral solution was set to $6 \cdot 10^{-10} \text{ m}^2/\text{s}$ [6]. Velocity maps, concentration maps and pressure drop of the entire delivery system were evaluated.

III. RESULTS

The transient simulation of the first part of the domain, that is the inlet tube fed with dopamine, allowed to obtain concentration profiles at the outlet. These profiles were given as boundary condition for the connector part. Figure 3b shows velocity map and dopamine concentration map on the symmetry plane for the connector when the condition of stationarity is reached. It is noticeable that due to the huge difference between the flow rates at the two inlets ($Q_C/Q_D = 100$), the drug is squeezed toward the wall of the channel, where the velocities are extremely slow (Fig. 3a). Therefore the drug is not optimally carried through the channel, and the time needed for the drug to go through the entire length of inlet tubing and connector is considerably long. The expected time calculated with (1) is equal to $t = 20$ minutes, while the time estimated from the simulation is equal to $t = 50$ minutes. About 30 minutes are required for the drug to completely fill

the inlet tube, while 20 minutes is the time needed to go through the connector. Therefore, a 30 minutes delay occurs with respect to the theoretical value, and this is likely to be caused both by the segregation between carrier fluid and drug and by the presence of a dead volume inside the four-port connector which slows significantly the process.

The pressure drop along the entire system is very low ($\Delta P \approx 80 \text{ Pa}$).

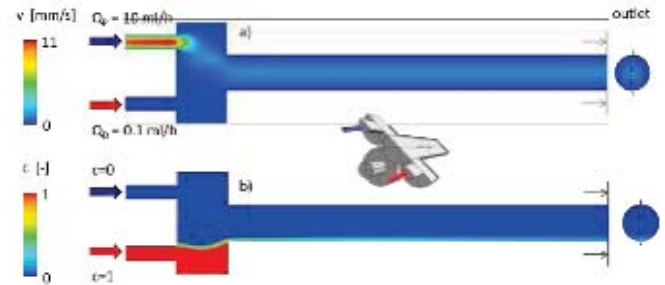


Fig. 3. Velocity and concentration maps on the symmetry plane and on the outlet of the four-port connector.

IV. CONCLUSION

Current infusion techniques in the pediatric care setting can result in significant, unrecognized, and potentially hazardous delays in achieving delivery of intended drugs doses to the patient. In our study, we analyzed the pediatric infusion system currently in use at A. Manzoni hospital in Lecco. We found out that a significant delay in the delivery of the drug occurs. This suggests that subtleties in the design and use of the connections can impact the dynamics of drug infusion and warrant further investigations.

V. ACKNOWLEDGMENTS

The authors kindly acknowledge doctors and nurses of the neonatal unit of the A. Manzoni Hospital in Lecco.

REFERENCES

- [1] D.R. Moss, K. Bartels, G. Peterfreund, M.A. Lovich, N.M. Sims, R.A. Peterfreund, "An in vitro analysis of central venous drug delivery by continuous infusion: the effect of manifold design and port selection," *International Anesthesia Research Society*, vol. 109, pp. 1524-1529, 2009
- [2] D.S. Levi, N. Peterson, S.D. Shah, B. Rakholia, A. Haught, G. Carman, "Connecting multiple low-flow intravenous infusions in the newborn: Problems and possible solutions," *Pediatric Critical Care Medicine*, vol. 11, pp. 275-281, 2010
- [3] K. Bartels, D. R. Moss, R. A. Peterfreund, "An analysis of drug delivery dynamics via a pediatric central venous infusion system: quantification of delays in achieving intended doses," *Anesth Analg*, vol. 109, pp. 1156-1161, 2009
- [4] M.A. Lovich, M. E. Kinnealley, N. M. Sims, R. A. Peterfreund. "The Delivery of Drugs to Patients by Continuous Intravenous Infusion: Modeling Predicts Potential Dose Fluctuations Depending on Flow Rates and Infusion System Dead Volume" *Anesth. Analg.*, vol. 102, pp. 1147-1153, April 2006
- [5] M. A. Lovich, J. Doles, R.A. Peterfreund, "The impact of carrier flow rate and infusion set dead-volume on the dynamics of intravenous drug delivery," *Anesth. Analg.*, vol. 100, pp. 1048-1055, April 2005
- [6] G. Zou, Z. Liu, C. Wang, "Flow injection analysis methods for determination of diffusion coefficients," *Analytica Chimica Acta*, vol. 350, pp. 359-363, 1997

Buoyancy driven flows in a microfluidic device for PCR applications

E. Bianchi¹, F. Nason¹, M. Cioffi and G. Dubini¹

¹ Structural Engineering Department, Politecnico di Milano, Piazza Leonardo Da Vinci 32, 21100 Milano Italy

Abstract— Polymerase Chain reaction is a widespread thermic process that consists in the *in vitro* amplification of a DNA samples: it plays a central role in the molecular biology. The miniaturization of PCR systems is promising as it potentially minimizes the reagent consumption and, combined with a fluid flow strategy to handle the sample, increases the reaction rate and reduces the thermal inertia. In such a system sample solution is usually handled by external pumps: an alternative solution relies on temperature-induced density difference in the presence of a body force to induce buoyancy driven flow. This alternative is an easy-to-use method and does not require expensive set-up, but, to date, still needs to be optimized: temperature and flow fields are influenced together to the geometry of the microfluidic channel, hosting the sample. The present study focuses on the design of cycle channel and on the evaluation of the impact of the temperature field and of the geometrical features to the quality of the buoyancy driven flow.

Keywords—PCR, Polymerase chain reaction microfluidics, buoyancy driven flow.

I. INTRODUCTION

Proposed by Kary Mullis in 1983, polymerase Chain Reaction (PCR) it is a powerful tool for creating large numbers of copies of specific DNA fragments for applications like DNA fingerprinting, genomic cloning and genotyping for disease diagnosis [1].

In the common devices used for PCR, sample continually thermally cycled between three distinct temperatures for denaturation (90-94 °C), annealing (50-60 °C) and extension (72 °C).

Bench top thermal cyclers can generally be classified into two categories: the chamber type, where the DNA sample is placed and thermally cycled, and the continuous flow type, which consists of micro-channels continuously looped through different temperature zones.

The continuous flow type has the important advantage of being able to guarantee better thermal management, which is crucial for the get the target amplification: this positively affects amplification time reduction [2].

However in a continuous flow PCR device the ratio surface to sample volume is huge, causing the loss of sample along the channel. As well a continuous flow device requires external pumping and has a fixed number of thermal cycles.

Some alternative solutions have been recently developed, relying on a temperature-induced density difference in the presence of a body force to induce buoyancy-driven flow [3,4]. This alternative method is easy to use and does not require expensive set-up, but, to date, further efforts should be taken to optimize the thermo-fluid-dynamic field in the

micro-channels. The influence of the temperature field on the generated flow has been investigated with a parametric analysis on the micro-channel geometry.

II. MATERIALS AND METHODS

A three dimensional microchannel was arranged in a closed loop (Fig. 1): different combinations of microchannel square cross-sections ($W = 500, 400, 300$ and $200 \mu\text{m}$), and device length ($L = 3, 4$ and 5 mm) were modelled.

A CAD modeller (Ansys Inc., Canonsburg, PA, USA) was used to set up the models and build the meshes. Two domains were built for each geometry configuration: the fluid domain, within the microchannels, was considered to have the same properties as an aqueous solution ($c_p=4180 \text{ J kg}^{-1} \text{ K}^{-1}$, $k=0.684 \text{ W m}^{-1} \text{ K}^{-1}$). The solid domain, in the centre of the device, consisted of a polymeric material, having the same properties as poly-dimethylsiloxane (PDMS $c_p=1460 \text{ J kg}^{-1} \text{ K}^{-1}$, $k=0.15 \text{ W m}^{-1} \text{ K}^{-1}$). Geometries were discretized with about 70k – 500k elements, resulting from sensitivity and optimization analyses.

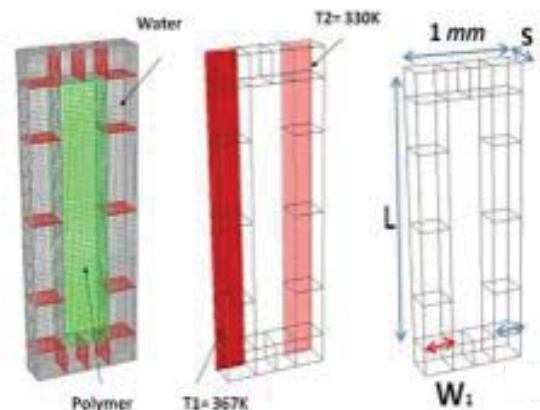


Fig. 1. (a) Computational domain: fluid domain (grey) and solid domain (green); (b) Thermal boundaries: heaters on the backside of the device; (c) geometrical parameters: thickness S is equal to the width W_1 in each configuration.

Steady-state simulations were carried out using the finite volume code FLUENT (Ansys Inc., Canonsburg, PA, USA). The Navier-Stokes equations for Newtonian fluids were solved in the fluid domain: respectively; μ_t and ρ_t are respectively the viscosity and the density of the fluid as functions of the temperature T .

Gravitational acceleration was considered to be 9.81 m s^{-2} parallel to L dimension. No-slip conditions were imposed at the walls. Heater location was simulated by imposing

constant temperature boundary conditions (T_1 and T_2 , 367 K and 330 K respectively) on one side of the device (Fig. 1). Thermal continuity was applied at the wall between the micro-channel and the PDMS core. Thermal resistances were applied at the other boundaries, so as to simulate conduction through a PDMS layer (2 mm on the frontal and back sides, normal to the X axis, and 5 mm in thickness on the other sides) and the external environment (air at 297 K with a convection coefficient $h = 5 \text{ W m}^{-2} \text{ K}^{-1}$).

III. RESULTS AND DISCUSSION

The computational analysis of the thermal cycle showed that a significant increase in the flow velocity – thus a reduction of the time required for a single cycle – may be achieved by widening the channel cross section. Also increasing channel length leads to an increase of the flow velocity, but it also increases the length of the cycle. For the considered channel lengths, this results in an increase of the time required for a cycle.

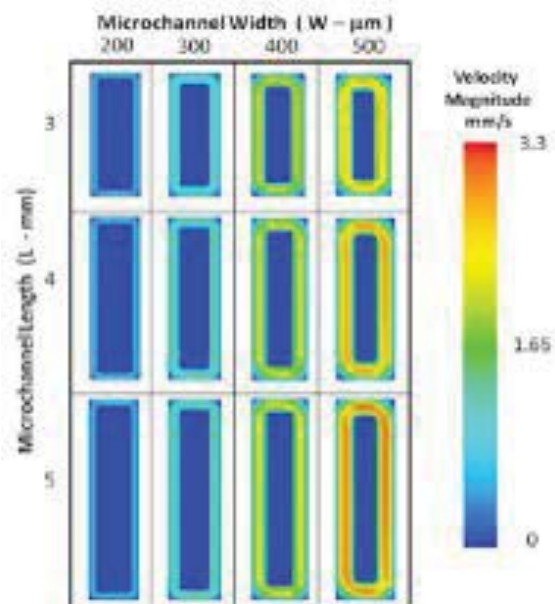


Fig. 2 Velocity magnitude contours on the middle cross-sectional plane of the designed microdevices.

One might infer that the ideal device should minimize the time required for amplification, such as the devices with channel W equal to 500 μm and channel length equal to 5 - 4 - 3 mm, depending on the desired sample volume. These systems will allow for one cycle of amplification of 3 - 2.5 - 2 μL of DNA sample in less than 4 s. However such a configuration leads to a heterogeneous temperature distribution within the channels, which may prevent efficient DNA amplification (Fig.3).

Therefore we suggest to go for systems with smaller channel cross-sections, such as the microdevices with $W = 300 \mu\text{m}$ or $W = 200 \mu\text{m}$, selecting the most suitable priming volume or time to cycle (Table 1). These configurations allow the sample to reach and keep plateaus of temperatures more stable and longer in time, setting the conditions for a more efficient reaction.

IV. CONCLUSION

Computational fluid dynamic simulations were carried out to study buoyancy-driven flow phenomena inside a micro channel, conceived to allow the optimization of DNA sample amplification within PCR devices. Steady-state simulations were performed to identify the parameters affecting the duration and the timing of the thermal cycle.

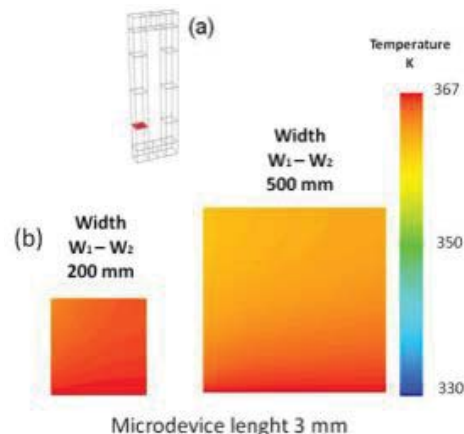


Fig. 3 Temperature contours (b) on a comparative cross section (a) in microdevice models with the same $L=3$ and different W .

	$W=200$	$W=300$	$W=400$	$W=500$
$L=3$	0.3 μL - 13s	0.75 μL - 6.5s	1.25 μL - 3.5s	2 μL - 3s
$L=4$	0.4 μL - 16s	0.9 μL - 7s	1.5 μL - 4.5s	2.5 μL - 3.5s
$L=5$	0.5 μL - 18s	1 μL - 8s	2 μL - 5s	3 μL - 4s

Table. 1 Priming volume and time to cycle for each configuration. The maximum flow velocity in the channel section has been considered.

As expected, both the width of the channel cross section W and the length of the channel L increased the flow velocity. The results of this study can help choosing a few geometry configurations, which potentially optimize the performance of a PCR microdevice, reducing the cycle time and the priming volume, with homogeneous distribution of temperature within the channel cross sections and an optimized time ratio to each temperature zone. Future developments of this study should mainly address the optimization of microdevice geometry, for the case with the introduction of a third thermal condition (extension at 72 $^{\circ}\text{C}$) and the introduction of asymmetric geometries to better assess the permanence of the sample to the different temperature and the temperature gradients.

REFERENCES

- [1] K. Mullis 1990. *The unusual origin of the Polymerase Chain Reaction*. Scientific American, pp. 56-65
- [2] N. Parl, S. Kim, J. H. Hahn 2003. *Cylindrical compact thermal cycling device for continuous-flow polymerase chain reaction*. Anal Chem. 75 pp. 6029-6033
- [3] E.K. Wheeler, W. Benett, P. Stratton, J. Richards, A. Chen 2004. *Convectively driven polymerase chain reaction thermal cyclers*. Anal Chem. pp. 75- 76.
- [4] M. Krishnan, N. Agrawal, M. A. Burns, V. M. Ugaz 2004. *Reactions and Fluidics in Miniaturized Natural Convection Systems*. Anal Chem. Pp. 76, 6254-6265

Constitutive models for the investigation of biomechanical functionality of colon region

E.L. Carniel^{1,2} and A.N. Natali^{1,2}

¹ Department of Industrial Engineering, University of Padova, Padova, Italy

² Centre of Mechanics of Biological Materials, University of Padova, Padova, Italy

Abstract - The aim of the present work is to investigate the biomechanical behaviour of colon tissues by defining an appropriate constitutive formulation and a procedure for the parameters evaluation. The comparison of results with experimental data confirms the reliability of the analysis. This work is the basis of more comprehensive activities that aim at providing numerical tools for the interpretation of surgical procedures that refer to gastrointestinal tract, also considering the specific devices adopted.

Keywords - colon tissues, hyperelastic formulation, constitutive analysis, numerical models.

I. INTRODUCTION

NUMERICAL analysis of biological tissues with regard to surgery proved a relevant capability to support and integrate the operational procedures, mostly with regard to the mechanical aspects. Research efforts in minimally invasive surgery are driven through the improvement of locomotion ability and sensing efficiency of devices [1]. Models and experiments have been proposed to investigate the biomechanical aspects that must be considered in the design of procedures and devices to operate safely inside the abdominal region, but further efforts are mandatory for the definition of reliable numerical models that are suitable to actually interpret the functionality of biological structures during and after the surgical procedure. The essential tool for the development of reliable numerical models is the definition of constitutive formulations that actually interpret the mechanical response of the biological tissues. Such analysis requires a multi-disciplinary approach, accounting for information from histological investigation, data from mechanical testing, together with mathematical skills for the rigorous definition of constitutive models. Some notes are here reported about the constitutive analysis of colon tissues. The colon is a biological structure with a lumen surrounded by a four layers wall, as mucosa, submucosa, muscularis externa and serosa (Fig. 1).

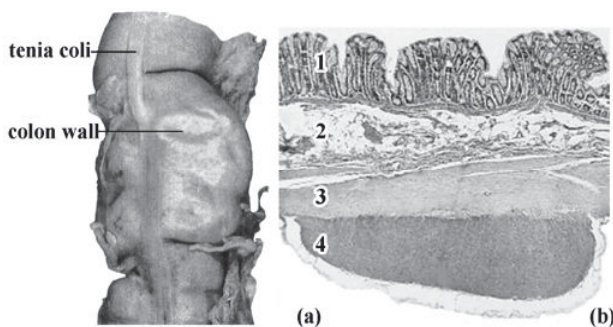


Fig. 1. Morphometric (a) and histological (b) configuration of the colon: mucosa (1), submucosa (2), muscularis externa (3) and tenia coli (4).

The mucosal inner layer is composed by connective tissue where thin collagen fibrils are organised according to a loose and random network. The submucosa is generally thicker than mucosa and mainly composed of a dense network of thick collagen fibres. In detail, two collagen fibres sets, arranged in a criss-cross pattern, can be identified, running respectively in clockwise and anticlockwise helices down the large intestine. In literature different values of the crossing angle that the fibres form with the circumferential direction are reported, showing a range between 30° and 65° [2]. The muscularis externa is mainly composed of smooth muscle cells and can be subdivided into two layers according to the main direction of the fibres. In the internal layer, the orientation is circumferential, in the external layer it is longitudinal. Within the colon wall, the longitudinal layer is substantially thinner than the circumferential one. The mechanical propulsive action along longitudinal direction is ensured by teniae coli, as thick bands of longitudinal muscular tissue. Finally, the serosa is a very thin layer of loose connective tissue. The complex configuration of the colon region determines relevant difficulties in the interpretation of the biomechanical response. Collagen and muscular fibres distribution causes the anisotropic configuration associated with a strongly non-linear geometric and material response. A specific hyperelastic formulation is developed aiming at an interpretation of the biomechanical behaviour. Constitutive parameters are evaluated by the minimization of the discrepancy between model results and experimental data from mechanical tests [1] adopting a coupled stochastic-deterministic procedure [3].

II. MATERIALS AND METHODS

A. Definition of the constitutive model

The colon wall mechanical response is interpreted by using an hyperelastic constitutive formulation. The model must account for contributions from the different layers, with particular regard to mucosa, submucosa and muscularis externa. Mucosa is characterized by isotropic mechanical behaviour, while the distribution of fibrous elements within submucosa and muscularis externa determines an overall anisotropic configuration. In detail, two main sets of fibres can be identified for submucosa, arranged according to clockwise and anticlockwise helices, while one fibers family is assumed for muscularis externa along circumferential direction. According to the theory of fibre-reinforced composite materials, the strain energy function is defined by different contributions from ground matrix and fibrous components [4]:

$$W(\mathbf{C}) = W_m(\mathbf{C}) + W_f^{sm}(\mathbf{C}, \mathbf{a}_0, \mathbf{b}_0) + W_f^{me}(\mathbf{C}, \mathbf{c}_0) \quad (1)$$

where W_m is the contribute of the ground matrix contained in the different tissue layers:

$$W_m(\mathbf{C}) = U_m(I_3) + \tilde{W}_m(\tilde{I}_1, \tilde{I}_2) \quad (2)$$

$$U_m(I_3) = \frac{K_v}{2+r(r+1)} \left[(I_3^{1/2} - 1)^2 + I_3^{-r/2} + rI_3^{1/2} - (r+1) \right] \quad (3)$$

$$\tilde{W}_m(\tilde{I}_1, \tilde{I}_2) = [C_1/\alpha_1] \left\{ \exp[\alpha_1(\tilde{I}_1 - 3)] - 1 \right\} \quad (4)$$

W_f^{sm} is the anisotropic contribution caused by collagen fibres of submucosa, which are oriented according to local directions \mathbf{a}_0 and \mathbf{b}_0 :

$$W_f^{sm}(\mathbf{C}, \mathbf{a}_0, \mathbf{b}_0) = W_a(I_4) + W_b(I_6) \quad (5)$$

$$W_a(I_4) = [C_4/(\alpha_4)^2] \left\{ \exp[\alpha_4(I_4 - 1)] - \alpha_4(I_4 - 1) - 1 \right\} \quad (6)$$

$$W_b(I_6) = [C_6/(\alpha_6)^2] \left\{ \exp[\alpha_6(I_6 - 1)] - \alpha_6(I_6 - 1) - 1 \right\} \quad (7)$$

where $C_4 = C_6$ and $\alpha_4 = \alpha_6$ as parameters associated to fibres families that are characterised by different distribution but similar structural configuration and mechanical behaviour.

W_f^{me} is the anisotropic contribution of muscular fibres of muscularis externa, which are oriented along circumferential direction \mathbf{c}_0 :

$$W_f^{me}(\mathbf{C}, \mathbf{c}_0) = W_c(I_{10}) \quad (9)$$

$$W_c(I_{10}) = \frac{C_{10}}{(\alpha_{10})^2} \left\{ \exp[\alpha_{10}(I_{10} - 1)] - \alpha_{10}(I_{10} - 1) - 1 \right\} \quad (10)$$

B. Evaluation of constitutive parameters

Constitutive parameters are evaluated comparing model and experimental results by a fitting procedure. In order to achieve a complete and reliable set of parameters, data from different experimental tests are necessary, under tensile and shear loading along different directions. Data from Ciarletta et al. [2] were assumed. They reported results from uniaxial tensile and shear tests, performed on pig specimens, according to both longitudinal and circumferential directions.

The first step of the procedure for parameters evaluation pertains to the development of analytical models to interpret the experimental tests, accounting for the constitutive formulation and the specific boundary conditions. The discrepancy between experimental and model results is evaluated by a cost function that depends on constitutive parameters. The minimization of the cost function, using a coupled stochastic-deterministic procedure, entails the definition of the optimal set of constitutive parameters [3].

III. RESULTS

The comparison of model and experimental results is reported in Fig. 2 to show the capability of the proposed constitutive formulation to interpret the mechanical response of colon wall. In detail, data from tensile and shear tests are reported. Both loading situations are investigated along circumferential and longitudinal directions.

IV. CONCLUSION

The model results follow the same trend of experimental data and highlight the capability of the constitutive formula-

tion developed of describing the mechanical behaviour of colon wall tissues. Similar formulations can be adopted to interpret the biomechanical response of tissues from other gastrointestinal organs.

Further experimental efforts should be necessary for a more accurate characterization of tissues biomechanical behaviour to account for inelastic phenomena related to viscous and damage response.

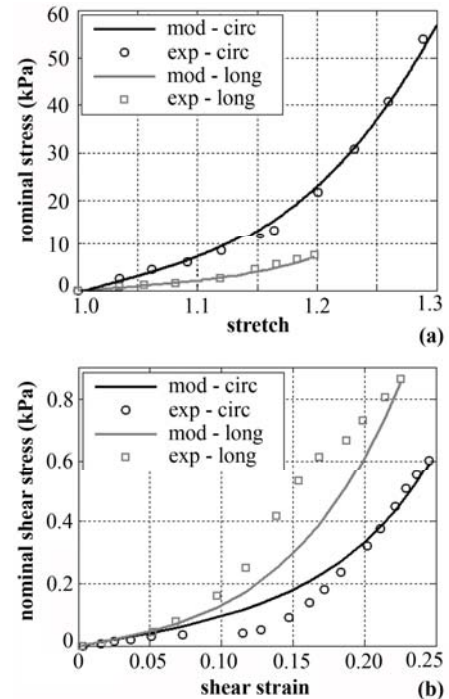


Fig. 2. Comparison of experimental (empty circles and squares) and model (continuous lines) results for tensile (a) and shear (b) tests on colon wall.

The analysis of biomedical images from CT and MRI reliefs leads the development of virtual solid models of the gastrointestinal region. Such models, together with the provided constitutive formulations, make it possible to define numerical models of gastrointestinal organs. Numerical analyses can be performed to investigate the functional response of the biological structures accounting also for tissues degenerative conditions determined by pathologies and/or aging. Furthermore, numerical methods allow to investigate tissues response with regard to the effects of surgical procedures, making it possible to evaluate mechanical aspects of surgical practices and specific devices adopted at the purpose.

REFERENCES

- [1] P. Ciarletta, P. Dario, F. Tendick and S. Micera, "Hyperelastic model of anisotropic fiber reinforcements within intestinal walls for applications in medical robotics", *The International Journal of Robotics Research*, vol. 28 (10), pp. 1279-1288, 2009.
- [2] G. Gabella, "The cross-ply arrangement of collagen fibres in the submucosa of the mammalian small intestine", *Cell Tissue Res*, vol. 248, pp. 491-497, 1987.
- [3] A. N. Natali, A. Forestiero and E. L. Carniel, "Parameters identification in constitutive models for soft tissue mechanics", *Russian J Biomech*, vol. 13(4), pp. 29-39, 2009.
- [4] A.N. Natali, E.L. Carniel and H. Gregersen, "Biomechanical behaviour of oesophageal tissues: material and structural configuration, experimental data and constitutive analysis", *Medical Engineering & Physics*, vol. 31, pp. 1056-1062, 2009.

Design and characterization of a non-homogeneous elastosonographic breast phantom using PVA-C

S. Celi^{1,2}, and G. L. Di Girolamo^{3,4}, and D. Della Latta³, and D. Chiappino³

¹ *Institute of Clinical Physiology, CNR, Heart Hospital, Massa, Italia*

² *Fondazione Toscana "G. Monasterio", CNR, Heart Hospital, Massa, Italia*

³ *Fondazione Toscana "G. Monasterio", CNR, Unit of Diagnostic Imaging, Heart Hospital, Massa, Italia*

⁴ *Dep. Chem. Eng. Mat. Science, University of Pisa, Pisa, Italia*

Abstract—Tissue stiffness measurements performed with elastosonography have the potential to offer an additional procedure for diagnosing breast lesions in a non-invasive manner. However the interpretation of the elastogram, to date, still remains difficult. Tissue-mimicking phantoms are useful in the field of tissue characterization and can be essential in elastosonography for the purpose of training the operator and for the validation of computational models. This study is dedicated to the design and characterization of polyvinyl alcohol cryogel (PVA-C) for breast phantoms for these types of applications.

Keywords—Elastosonography, Breast phantom, PVA-C, Mechanical characterization.

I. INTRODUCTION

ELASTOSONOGRAPHY (ES) is a technique that correlates the ultrasound (US) Radio-Frequency signals to the strain field of the biological tissues [1]. In ES the echographic probe has the double function of US transducer and mechanical actuator. The ES technique is able to identify pathological tissue starting from the observation that the mechanical properties of tissues are generally correlated with pathological changes; in particular some cancerous lesions are characterized by an increased stiffness. ES procedure for breast exam, in particular, is non-invasive, non-ionizing and highly tolerated by patients; however it is considered not enough reliable mainly due to the difficulties in the interpretation of the elastogram (strain map). Despite the recent studies from both the imaging [2] and computational point of view [3], there is a lack of realistic breast phantoms for testing and benchmarking different algorithms. Moreover tissue-mimicking phantoms are essential for the training of the operator. To date, phantoms are mainly based on homogenous materials, consequently the comparison of the results with real cases, that are characterized by a high non-homogeneity, can be difficult. One of the challenges is to find materials that can mimic different tissue properties over a wide range of material properties and show similar dispersive behavior. The aim of the current work is to investigate the use of poly(vinyl alcohol) cryogel (PVA-C) as a tissue mimics material (TMM) for breast elastosonography.

II. MATERIAL AND METHODS

The starting point for the proposed phantom is based on previous published studies where the ultrasonographic properties of the PVA-C were analyzed [4]. PVA-C was chosen for the

phantom design for its biological tissue-mimicking properties [5]. The stiffness properties of PVA-C can be manipulated by processing the solution through a number of freeze/thaw cycles or varying the PVA concentration. First, different PVA-C were obtained, then mechanical tests were performed and finally different phantoms were created by changing tissue composition in terms of layers dispositions and dimensions.

A. PVA-C preparation

99% hydrolysed poly(vinyl alcohol) powder (Sigma-Aldrich) was chosen to make the PVA liquids due to its high level hydrolysis. In order to mimic both soft and hard tissue three types of cryogels have been prepared: 5% (PVA-C₅), 10% (PVA-C₁₀) and 15% (PVA-C₁₅) by weight of PVA, respectively. The PVA powder was mixed with de-ionised water and maintained in autoclave for 40 minutes (1 atm, 121°C) in order to achieve complete dissolution. Gelation of PVA samples were induced by one freezing-thawing cycle at -80C for 18 h. This freezing phase was chosen, after preliminary tests, in order to induce a suitable gelation in the PVA-C samples.

B. Mechanical test

Uniaxial tensile tests were performed on each PVA-C samples. Tests were performed in displacement control in a quasi-static condition on a testing machine presents in our laboratory. Samples were tested after 24 h from the freezing cycle. To calculate the strain, by avoiding the slippage of the samples in the grips, a specific optical extensometer, developed in Matlab, was used [6] by positioning calibrated markers ($\phi=0.39$ mm) along the sample; at least 5 markers were used to cope the local deformations. Moreover, the initial tangential Young's moduli (E_0) were calculated as the slopes of the stress-strain curves in the range of 0-10%.

C. Phantom design

The breast phantom was made by alternating layers of PVA-C in order to mimics the different tissue layers: fibro-glandular, glandular and fatty. Finally inclusion were gently positioned in the center of the fibrous-glandular layers by making an incision at the bottom of the phantom. A schematic draw of the breast phantom is reported in Figure 1. The thickness for

each layers were 10 mm, 10 mm and 50 mm for fatty/adipose, glandular and fibrous layers, respectively. The color bar depicts the different stiffness of the breast phantom layer from a hard to soft material.

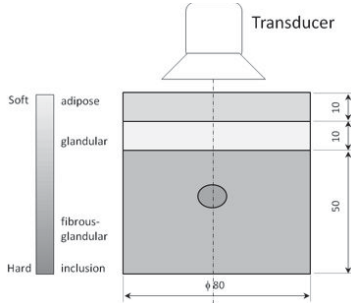


Fig. 1. Schematic representation of the cylindrical phantom. For clarification also the transducer probe is reported.

To simulate hard lesions, ellipsoidal inclusions (minor axis equal to 4 mm and major axis equal to 7 mm) of Poly(methyl methacrylate) (PMMA) were used. In order to reduce any air-gaps, the ES acquisitions were performed by placing the phantom in a filled water container and a commercial echographic gel was used between each layer.

III. RESULTS

Figure 2 shows stress-strain curves for the three different PVA-Cs, with their dispersion obtained from the analysis of each segments from of the optical extensometer data post-process.

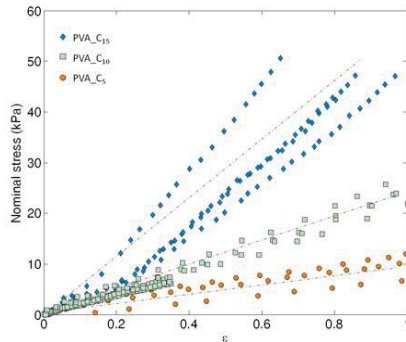


Fig. 2. Stress strain curves for the three different PVA-Cs. The dash-dot lines represent the mean behavior for each PVA-C.

The initial tangential moduli are reported in Table I. By comparing the E_0 values with those of the breast tissue, PVA-C₁₅ is correlated with fibrous/glandular, the PVA-C₁₀ with glandular and PVA-C₅ with fatty tissue. In fact, these results are in good agreement with experimental data reported in literature regarding breast tissues, in particular with Krouskop et al [7] for the fat and glandular layers. Indeed for the fibrous material, our data cover only a part of the published Young's moduli values.

It is worth to notice that for this type of material the E values range from 3.55 ut to 139 kPa, [3]. Our phantom, from

TABLE I
INITIAL TANGENTIAL MODULI

	PVA-C ₁₅	PVA-C ₁₀	PVA-C ₅
E_0 (kPa)	58 ± 7	30 ± 12	18 ± 8
TMM	fibrous/glandular	glandular	fat/adipose

the bottom to the top is composed by a layer of PVA-C₁₅ (Thk =50 mm), PVA-C₁₀ (Thk =10 mm) and PVA-C₅ (Thk =10 mm). In Figure 3 an example of quasi-static US imaging and ES exams on our breast phantom is reported. Four region of interest (ROI) were considered: ROI₁ in the PMMA, ROI₂ and ROI₄ in the PVA-C₁₅ and ROI₃ in the PVA-C₅.

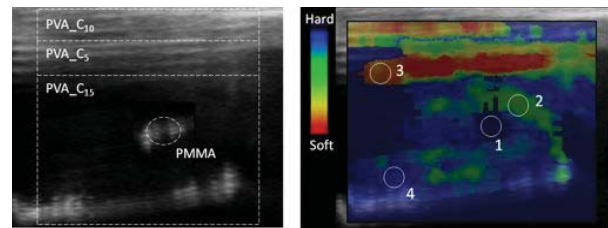


Fig. 3. B-mode image of hard inclusion encapsulated in a fibrous/glandular background (a), elastogram image (b). The white dash lines in the B-mode image represent the phantom layers for clarification.

IV. CONCLUSION

As general observation we can notice that the PVA-C is characterize by a non-homogeneous elastic material properties due to the peculiarities of its making process (freezing/thawing cycle). This breast phantom can serve as valuable intermediary between simple homogeneous phantom and real breast. Our ongoing activities are devote to perform also compression tests and to develop a suitable computation finite element models to help the comparison between real case and numerical phantom.

REFERENCES

- [1] J. Ophir and I. Céspedes and B. Garra and H. Ponnekanti and Y. Huang and N. Maklad, "Elastography: Ultrasonic Imaging of Tissue Strain and Elastic Modulus in Vivo," *Eur. J. Ultrasound*, vol.3, pp. 4970, 1996.
- [2] K. J. Parker, M. M. Doyley and D. J. Rubens, "Imaging the elastic properties of tissue: the 20 year perspective," *Phys. Med. Biol.*, vol. 56), pp. R1R29.
- [3] S. Celi and F. Di Puccio and P. Forte, "Advances in finite element simulations of elastosonography for breast lesion detection," *J. Biomech. Eng.*, vol. 133, pp. 081006, 2011.
- [4] J. Fromageau and J. L. Gennisson and C. Schmitt and R. L. Maurice, R. Mongrain and G. Cloutier, "Estimation of Polyvinyl Alcohol Cryogel Mechanical Properties with Four Ultrasound Elastography Methods and Comparison with Gold Standard Testings," *IEEE Trans Ultrason Ferroelect Freq Contr*, vol. 54(3), pp. 498-508, 2007.
- [5] C. M. Hassan and N. A. Peppas, "Structure and applications of poly(vinyl alcohol) hydrogels produced by conventional crosslinking or by freezing/thawing methods," *Adv. Polymer Sci.*, vol. 153, pp. 3765, 2000.
- [6] S. Celi, "Simulazione numerica e sperimentale di pratiche chirurgiche," PhD Thesis, Dep. Mech. Nucl Prod Eng, University of Pisa, 2008.
- [7] T. A. Krouskop and T. M. Wheeler and F. Kallel and B. S. Garra , T. Hall, "Elastic moduli of breast and prostate tissues under compression," *Ultrason Imaging*, vol. 20(4), pp. 260-274, 1998.

FE simulations on the effect of regional variations of material properties and wall thickness on AAA

S. Celi^{1,2}, and S. Berti²

¹ *Institute of Clinical Physiology, CNR, Heart Hospital, Massa, Italia*

² *Fondazione Toscana "G. Monasterio", CNR, Unit of Adult Cardiology, Heart Hospital, Massa, Italia*

Abstract—In recent years an interest in the analysis of aortic wall stress distribution from a biomechanical approach has been developed by means of finite element analyses, in particular the wall stress value and distribution has been investigated. However computational analyses are limited by the use of many simplifying assumptions such as constant wall thickness and no distinction between healthy and pathological tissues. In this study a novel computational model is presented where regional variations of wall thickness and material properties are taken into account.

Keywords—Aneurysms, Wall stress, Weighted non linear fitting, Anisotropy.

I. INTRODUCTION

IN literature it is well known that changes with age and pathological conditions lead to regionally vary the mechanical properties of the artery wall, [1]. The structural integrity of the abdominal aorta is maintained by elastin, collagen and vascular smooth muscle cells and, during aneurysm formation, the tissue exhibits a significant increase in stiffness and anisotropy with respect to healthy tissue (HAA). These structural changes are associated with a median wall thickness reduction in the aneurysmal regions ($\sim 50\%$). Moreover, [2] also noticed that in a ruptured abdominal aortic aneurysm (AAA) there is a dramatic reduction ($\sim 90\%$) from the posterior to the anterior region around the rupture site. From a computational point of view, to date, many constitutive models have been proposed to account for the distribution of collagen fibers, while only a few authors (see [3], [4]) have taken into account the effect of the wall thickness on the wall stress distribution. To date, to the best of our knowledge, no computation finite element (FE) models have been reported including the aforementioned local variation. The aim of this study is to present a novel analytical AAA model characterized by regional variations of both material properties and wall thickness to analyze their effect on the wall stress distribution. In this study, variations have been introduced between the necks and the bulge such as the ventral and dorsal regions.

II. MATERIAL AND METHODS

In this study three main packages can be distinguished. Firstly a novel AAA geometry has been extracted by analyzing CT images from our database. Then the anisotropic material properties of AAA, HAA and their transition region were obtained and defined. Finally the FE simulations were performed.

A. Morphological measurement and AAA geometry definition

A total of 67 CT datasets of human AAA without thrombus, that were being evaluated for endovascular repair, were investigated. Images were obtained on 64-slice CT with 0.5 mm thick detector collimation. The data were collected and used to develop a new AAA lumen profile. Our geometry model is able to independently describe the cross-section shape of the lumen (i), the maximum (ventral) and minimum (dorsal) bulge diameters (ii), the length of the aneurismatic region (iii), the lumen eccentricity (iv) and the wall thickness along the longitudinal and circumferential direction (v). Due to the difficulties of measuring the wall thickness from CT images, values from literature were assumed, [2].

B. Material model

The healthy and aneurismatic material properties were obtained by implementing the four-fiber-family (4FF), [5], Strain Energy Function (SEFs) by means of a specific USERMAT routine by using the material coefficients reported in [6]. The experimental dataset were obtained simulating biaxial tension tests with different loading ratio. Additionally, a third material (AHA) was able to characterize the transition region between HAA and AAA by simply manipulating the two data-sets, Figure 1.

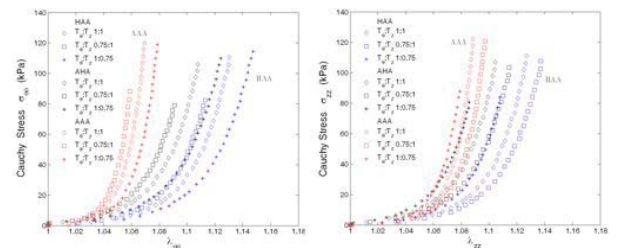


Fig. 1. Example of HAA and AAA material model and virtual dataset (AHA) for the transition region

The experimental data were used to fit 4FF. Moreover, in order to reduce the computational cost, a new structural based phenomenological two-fiber-family based on a polynomial form, was investigated. To enhance the fitting results, we have developed and implemented in Matlab a specific weighted non linear least squared (wNLS) procedure. Our weighted optimization routine is based on the Levenberg-Marquart algorithm and allows for the definition of a custom weight-function to force the fitting procedure in the high-stress

region of the mechanical behavior. Moreover in order to test the robustness of our fitting procedure, the experimental data were corrupted by noise insertion.

C. Finite Element models

The resulting solid models were meshed with hexaedral elements (SOLID185). Due to the nearly incompressible behavior of the materials, the \bar{B} and the $u - p$ formulation were adopted. Aneurysms were inflated applying a uniform pressure of 16 kPa and the ends of the models were left free to move in the radial direction. Figure 2 depicts an example of asymmetric AAA with a thickness (Thk) reduction of 30% in the bulge and of 20% in the dorsal region with respect to the Thk in the healthy necks ($Thk_{neck}=1.8$ mm).

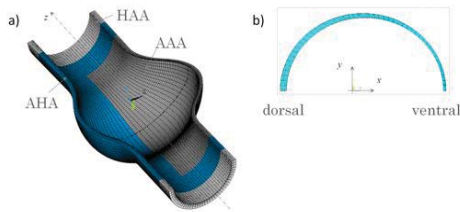


Fig. 2. Example of asymmetric aneurysm and assignment of local material properties (a) and transversal cross section (b).

For the definition of the anisotropy, the local fiber directions were located in each element centroid and oriented calculating each element curvature in both circumferential and axial direction (by the relative node coordinate). The sensitivity of the input parameters has been evaluated with respect to the maximum wall stress value and mapping.

III. RESULTS

In order to analyze the effectiveness of the proposed wNLS algorithm, in Figure 3 an example of fictitious experimental data and fitting result for a 4FF model is reported. The obtained value for the parameters are: $c = 1.1$ (kPa), $k_1^1 = 4.80$ (kPa), $k_2^1 = 17.18$, $k_1^2 = 3.74$ (kPa), $k_2^2 = 46.96$, $k_{3,4}^1 = 6.73$ (kPa), $k_{3,4}^2 = 53.13$, $\alpha = 40.04^\circ$. The resulting R^2 was calculated equal to 0.997. As we can observe, our fitting procedure, in particular, has increased the c value: this result helps significantly the convergence of the FE solution due to the maintenance of the isotropic component of the SEF.

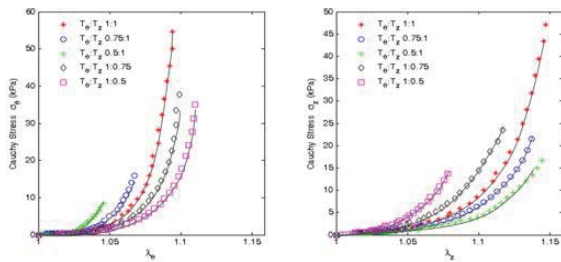


Fig. 3. Example of fitting results (solid lines) for a 4FF (AAA_{10} from [6]). Symbols indicate the experimental data from the biaxial test in Ansys.

As far as the polynomial 2FF, a 6 parameters constitutive model was sufficient to fit the dataset in Figure 1:

$$W_{2FF} = \sum_{a=1}^3 (\hat{I}_1 - 3)^a + 2 \sum_{c=4}^6 (\hat{I}_4 - 1)^c \quad (1)$$

where a_i and c_i are material coefficients, \hat{I}_1 is the first pseudo-invariant and \hat{I}_4 is the fourth pseudo-invariant.

Figure 4 depicts the circumferential stress for model (a) with an uniform thickness and one material model (AAA) and for a model with three different materials and wall thickness regional variation. Results show that and uniform Thk value and the use of only AAA material model underestimate the wall stress value of about 16%. Simulation results, not reported here for brevity, to analyse only the effect of the wall thickness reductions, showed an increase of the maximum stress of about 13% and of 22% in case of a 30% 50% Thk variation in the bulge, respectively.

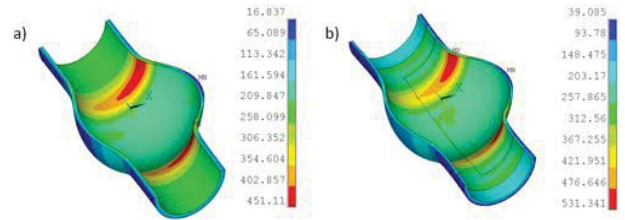


Fig. 4. Circumferential stress (kPa) for a model with constant Thk and one material (AAA) (a) and with regional variation of both Thk and material model (AAA, AHA and HAA) (b).

IV. CONCLUSION

A more complex computational model, in terms of wall thickness and material properties variations, can provide more realistic stress distribution, and, in particular can point out the parameters that mainly influence the wall stress. Our ongoing analysis are devoted to include a gradual material properties variation and to consider different SEFs implementation.

REFERENCES

- [1] D. Haskett and G. Johnson and A. Zhou and U. Utzinger and J. Vande Geest, "Microstructural and biomechanical alterations of the human aorta as a function of age and location," *Biomech Model Mechanical*, vol. 39(16), pp. 3010-6, 2006.
- [2] M. L. Raghavan and J. Kratzberg and E. M. Castro de Tolosa and M. M. Hanaoka and P. Walker and E. S. da Silva, "Regional distribution of wall thickness and failure properties of human abdominal aortic aneurysm," *J Biomech.*, vol. 9(6), pp. 725-36, 2010.
- [3] S. Celi and F. Di Puccio and P. Forte and M. Mariani and S. Berti, "Investigation on the effect of the wall thickness in rupture risk estimation of AAA by a probabilistic finite element approach," *European Heart Journal*, vol. 31(Supp)(1), pp. 284, 2010.
- [4] C. M. Scotti and A. D. Shkolnik and S. C. Muluk and E. A. Finol, "Fluid-structure interaction in abdominal aortic aneurysms: effects of asymmetry and wall thickness," *BioMedical Engineering OnLine*, vol. 4(64), pp. 22, 2010.
- [5] S. Baek and R. L. Gleason and K. R. Rajagopal and J. D. Humphrey, "Theory of small on large: Potential utility in computations of fluid-solid interactions in arteries," *J. R. Soc. Interface*, vol. 196(31), pp. 3070-3078, 2007.
- [6] J. Ferruzzi and D. A. Vorp and J. D. Humphrey, "On constitutive descriptors of the biaxial mechanical behaviour of human abdominal aorta and aneurysms," *J. R. Soc. Interface*, vol. 8(56), pp. 435-450, 2011.

Finite Element Analysis of Carotid Artery Stenting: from diagnosis to prediction

M. Conti^{1,*}, F. Auricchio^{1,2}, A. Ferrara¹, M. Ferraro^{1,2,*}, S. Morganti¹, A. Reali¹,

¹ *Dipartimento di Meccanica Strutturale, Università di Pavia, Via Ferrata 1, 27100 Pavia, Italy.*

² *Center for Advanced Numerical Simulations (CESNA), Istituto Universitario di Studi Superiori di Pavia (IUSS), V.le Lungo Ticino Sforza 56, 27100 Pavia, Italy.*

* *Corresponding author: Michele Conti, email: michele.conti@unipv.it*

Abstract—Stenosis of the carotid artery causes 20% of all ischemic strokes and transient ischemic attacks. The application of stenting for carotid artery revascularization is rapidly arising but its effectiveness is still a matter of debate. Design, development and performance assessment of the devices used in this procedure is the natural application field of (computational) biomechanics. The present study is collocated within this scenario and, in particular, we will discuss the impact of different stent designs on the vessel anatomy to assess quantitatively the relation between a given stent design and a given CA anatomy as a contribution to integration process between the computational tools and clinical practice.

Keywords—Finite Element Analysis (FEA); Carotid Artery Stenting (CAS); Patient-specific Modeling.

Cardiovascular diseases (CVDs) are nowadays the leading cause of death in the Western countries; they are often related to atherosclerosis, a degeneration of the vessel wall causing a number of events, ranging from arterial hardening to lumen narrowing (stenosis). In particular, stenosis of the carotid artery (CA) causes 20% of all ischemic strokes and transient ischemic attacks. Several treatment options are nowadays available for managing CA stenosis but the application of percutaneous minimally invasive techniques, such as stenting, for CA revascularization is rapidly arising.

Accordingly, carotid artery stenting (CAS) is a procedure which restores the vessel patency by enlarging the narrowed lumen by the expansion of a metallic mesh, which is driven to the target lesion through a endovascular catheter. Design, development and performance assessment of the devices used in this procedure are the natural application field of (computational) biomechanics. The present study is collocated within this scenario since it aims at investigating several aspects of CAS by means of numerical simulations, i.e., finite element analysis (FEA), and supporting the clinical practice through a quantitative assessment of the relation between the complex mechanical features of a given stent design and a given patient-specific anatomy.

In particular, the study will discuss the following items:

- impact of different stent designs on the vessel anatomy assessing quantitatively the relation between a given carotid stent design and a given patient-specific CA anatomy [1];
- validation of the numerical analysis with respect in-vitro experiments [2];
- constitutive modeling of the carotid tissue and inclusion

of the plaque [3] (see fig. 1);

- simulation post-processing to evaluate vessel straightening, lumen gain and stent cell area;
- comparison between the simulations and the real cases.

Bearing in mind the multidisciplinary nature of the proposed investigation, this study can be considered as a contribution to integration process between the computational tools and clinical practice, in order to support the procedure standardization.

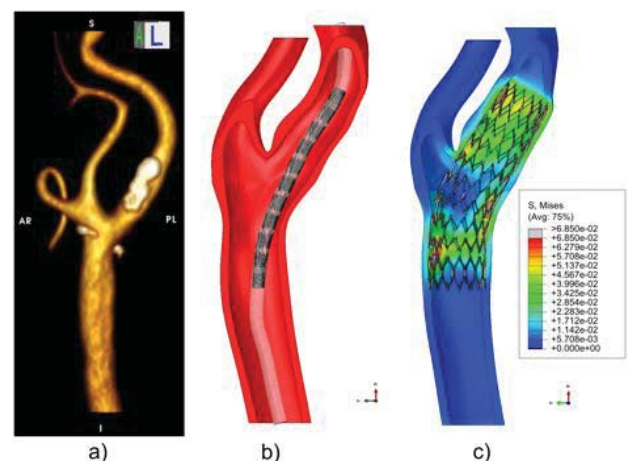


Fig. 1. FEA of CAS: a) 3D reconstruction of CA lumen from CTA images; b) stent crimped in the delivery system during the simulation; c) contour plot depicting the post-stenting stress distribution [MPa].

REFERENCES

- [1] F. Auricchio, M. Conti, M. De Beule, G. De Santis, and B. Verheghe. Carotid artery stenting simulation: from patient-specific images to finite element analysis. *Medical Engineering & Physics*, 33:281–289, 2011.
- [2] M. Conti, D. Van Loo, F. Auricchio, M. De Beule, G. De Santis, B. Verheghe, S. Pirrelli, and A. Odero. Impact of carotid stent cell design on vessel scaffolding: a case study comparing experimental investigation and numerical simulations. *Journal of Endovascular Therapy*, 18:397–406, 2011.
- [3] F. Auricchio, M. Conti, A. Ferrara, and A. Reali. Finite element analysis of carotid artery stenting: Impact of constitutive vessel modeling on vessel wall stress distribution. *CMBE2011 conference proceedings*, pages 367–370, 2011.

Non-Linear QCT-based FE models predict in vitro femoral strength better than DXA

E. Dall'Ara¹, B. Luisier¹, M. Pretterklieber², F. Kainberger³, P. Zysset⁴, D. Pahr¹

¹ Institute of Lightweight Design and Structural Biomechanics, Vienna University of Technology, Austria

² Department of Applied Anatomy, Center of Anatomy and Cell Biology, Medical University of Vienna, Vienna, Austria

³ Department of Radiology, Medical University of Vienna, Austria

⁴ Institute for Surgical Technology and Biomechanics, University of Bern, Switzerland

Abstract—Osteoporotic femoral fractures are a major clinical problem. DXA is the current clinical surrogate for femoral strength. QCT-based finite element (FE) analysis is a powerful tool for prediction of bone strength. The aim of this study was to validate a nonlinear FE model against experiments for the human proximal femur and to compare its prediction ability with densitometric measures. The FE models showed better predictions of ultimate force and stiffness compared to DXA ($R^2=0.80$ and $R^2=0.83$ for FE vs $R^2=0.26-0.66$ for densitometric parameters) but underestimated the experimental ultimate force. Moreover, the predicted damage distribution was qualitatively consistent with the femoral failure *in vitro*.

Keywords—Finite Element, Human Femur, Experiment, Bone Mineral Density.

I. INTRODUCTION

FEMORAL fractures among the elderly are a major public-health problem associated with high mortality and drastic reduction of quality of life. The better understanding of the mechanical resistance of the femur in a one-legged stance configuration is interesting to study spontaneous fractures (associated to a reduction of bone mineral density (BMD) in osteoporotic subjects) [1]. Dual energy X-rays absorptiometry (DXA) is used in clinics to measure BMD and bone mineral content (BMC) in the femur and in the spine. However, densitometric measures have shown moderate correlations with femoral strength. On the other hand, several FE models based on quantitative computer tomography (QCT) images have been shown to predict bone strength with relatively high correlations [2]. However, each novel FE model has to be validated through *in vitro* experimental tests before using it for evaluation of femoral strength *in vivo*. The goal of this study was to validate a non-linear QCT-based FE model for the human femur in one legged stance configuration and to compare their femoral strength prediction ability with the one of densitometric measures.

II. MATERIAL AND METHODS

A. Sample Preparation

Left or right fresh frozen anatomic specimens of human femora were extracted from 38 voluntary bony donators (18 males, 20 females with age 77 ± 12 years, range 46-99) in agreement with the ethical commission of the Vienna Medical University. The bone tissue was kept frozen at -20°C until the beginning of the sample preparation and in between the procedure steps. The proximal portion of each femur was isolated by cutting at 80 mm distally to the middle point of

the lesser trochanter, perpendicularly to the proximal shaft axis. Polyurethane (PU) was used to embed the most distal 60 mm of the isolated proximal femur.

B. DXA measurements and QCT scans

Each sample was then submerged in 0.9% NaCl saline solution, exposed to vacuum for 10 minutes to remove air bubbles and scanned with DXA (*Discovery QDR, Hologic Inc., USA*) in a custom made chamber. Total, neck, trochanter and intertrochanteric BMD and BMC were computed with the standard procedures used in clinics.

Each sample was then scanned in the same chamber with a QCT (*Brilliance64, Philips, Germany*; in-plane resolution: 0.33 mm; slice thickness: 1 mm) together with a calibration phantom and the HU scale was converted into equivalent BMD scale (in mgHA/cc).

C. Mechanical Testing

The load was applied in the plane containing both proximal shaft and neck axis with an inclination of 20° from the proximal shaft axis. The most superior 10mm of the femoral head were embedded to distribute the load during the test. The embedding of the shaft was completely constrained. Furthermore, a custom made bearing allowed the two translations and the rotation in the plane perpendicular to the load axis. A servo-hydraulic testing machine (*Mini-Bionix, MTS system, U.S.A.*) was used to preload the femur with 50N and compress it at a rate of 5mm/min until failure was clearly visible. The axial force was measured by means of a 100kN load cell (*U3 force transducer, HBM, Germany*).

D. Voxel Finite Element Models

The QCT images were rotated to reproduce the femoral position in the experiments and then coarsened to 3 mm in side length isotropic voxels, which were directly converted to hexahedral elements. The images were cropped at the level of the embedding of the shaft and the embedding of the femoral head was modeled as in the experiments. The nodes of the most distal part of the shaft were fixed. The nodes on the top of the embedding were coupled to a node placed in the middle point of the top nodes of the femur. A displacement equal to 5 mm was applied along the axial direction. The other five degrees of freedom were not constrained to simulate the freedom guaranteed by the bearing and the relative rotation between the femoral head and the embedding (allowed by the cartilage layer) in the experiments.

The procedure proposed by Dall'Ara et al [3] was used on three more femora scanned with QCT and μ CT to compute bone volume fraction (BV/TV) from BMD:

$$BV / TV = 0.093 * BMD + 1.080 \quad (1)$$

An elastic-damage constitutive model for bone developed by Garcia et al. [4] was used to model material non-linearity when it is loaded beyond a piecewise Hill criterion. In this model, damage [5], is included as a scalar variable (between 0 and 1) that describes the reduction of the elastic properties of the material. Bone elastic and strength properties were adapted from Rincon et al. [6] who performed multiaxial mechanical testing of trabecular bone from different anatomical sites. As cortical bone plays an important role in the femur, the bone material parameters were continuously extended to an elastic modulus equal to 24.129 GPa, compressive strength equal to 260 MPa and tensile strength equal to 200 MPa for BV/TV=1. In the lack of fabric information, bone was assumed isotropic. PU was modeled as an isotropic material with Poisson's ratio equal to 0.3 and Young's modulus equal to 1.36 GPa. Ultimate load and stiffness were calculated as the maximum load and the slope of the linear part of the "load - displacement" curves for both experiments (Exp_Fu and Exp_S) and models (vFE_Fu and vFE_S).

III. RESULTS AND DISCUSSION

Experiments reproduced typical femoral fractures: subcapital (N=13), neck (N=15) and intertrochanteric (N=6). In the remaining four cases the fracture was unclear and will be evaluated radiographically. The average femoral Exp_Fu (8.38 ± 2.94 kN, range: 2.57-14.42 kN) and Exp_S (6.33 ± 2.05 kN/mm, range: 2.89-10.42 kN/mm) were in line with the results shown in the literature [2], [7]. A good correlation was found between experimental stiffness and ultimate force ($R^2=0.76$). Low correlation was found between bone strength and age ($R^2=0.31$).

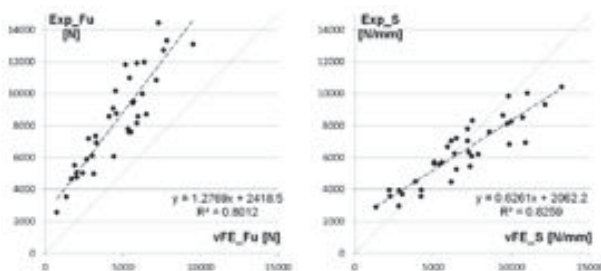


Fig. 1. Prediction of ultimate force and stiffness with vFE.

Average BMD and BMC values for total (0.71 ± 0.21 mg/cc and 30.6 ± 10.8 g), neck (0.60 ± 0.16 mg/cc and 3.4 ± 1.3 g), trochanteric (0.54 ± 0.19 mg/cc and 7.5 ± 3.2 g) and intertrochanteric (0.84 ± 0.24 mg/cc and 19.7 ± 7.0 g) regions were in line with previous studies [8]. Neck BMC ($R^2=0.66$) and Troch BMD ($R^2=0.44$) were the best predictors of Exp_Fu and Exp_S among the densitometric variables (in the other cases: $R^2=0.53-0.64$ for Exp_Fu and $R^2=0.26-0.43$ for Exp_S).

vFE_Fu and vFE_S predicted Exp_Fu and Exp_S ($R^2=0.80$ and $R^2=0.83$, Fig.1) better than densitometric parameter. Underestimation of the ultimate force (SI=1.28, Int=2.42 kN) might be due to the partial volume effect spreading and reducing the material properties of the cortex, which were not tuned to fit the experiments. The differences between predicted and experimental stiffness (SI=0.63, Int=2.06 kN/mm) might be due to the same effect as above and to the underestimation of Exp_S due to the compliance of machine, cartilage and PU. The damage distribution predicted qualitatively well the failure location (Fig.2).

Further work is necessary to evaluate the Exp_S by accounting for setup compliance and to assign suitable elastic and yield bone properties of the cortex to obtain a 1:1 prediction of the experimental results.

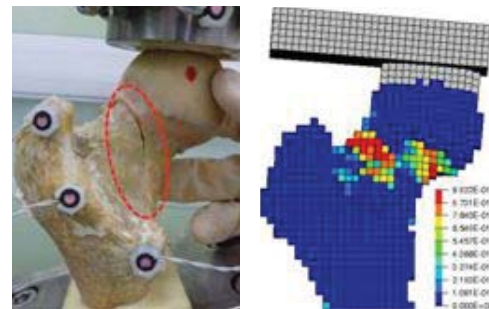


Fig. 2. Example of prediction of failure location with vFE

IV. CONCLUSION

In this study, a non-linear QCT-based FE model was validated versus experiments for the human proximal femur in one-legged stance configuration. The FE models predicted femoral ultimate force and stiffness better than densitometry *in vitro* and showed qualitative agreement with femoral failure location. The application of these models *in vivo* will be exploited in further studies.

REFERENCES

- [1] M. Viceconti, F Taddei, L. Cristofolini, S. Martelli, C. Falcinelli, and E. Schileo, "Are spontaneous fractures possible? An example of clinical application personalised, multiscale neuro-musculo-skeletal modelling," *JBiomech*, vol. 2, pp. 421-427, Feb 2012
- [2] J. Keyak, "Improved prediction of proximal femoral fracture load using nonlinear finite element models," *Med Eng Phys*, vol. 23, pp. 165-173, Apr 2001
- [3] E. Dall'Ara, P. Varga, D. Pahr and P. Zysset, "A calibration methodology of QCT BMD for human vertebral body with registered micro-CT images," *Med. Phys.*, vol. 38, pp. 2602-2608, May 2011
- [4] D. Garcia, P. Zysset, M. Charlebois and A. Curnier, "A three dimensional elastic plastic damage constitutive law for bone tissue," *Biomech Model Mechanobiol.*, vol. 8, pp. 149-65, Apr 2009
- [5] P. Zysset and A. Curnier, "A 3D damage model of trabecular bone based on fabric tensor," *JBiomech.*, vol.29, pp. 1549-1558, Dec 1996
- [6] L. Rincon-kohli and P. Zysset, "Multi-axial mechanical properties of human trabecular bone" *Biomech Model Mechanobiol.*, vol. 8, pp. 195-208, Jun 2009
- [7] L. Cristofolini, M. Juszczak, S. Martelli, F. Taddei and M. Viceconti, "In vitro replication of spontaneous fractures of the proximal human femur," *JBiomech*, vol. 40, pp. 2837-2845, 2007
- [8] E. Lochmueller, P. Miller, D. Buerklein, U. Wehr, W. Rambeck and F. Eckstein, "In Situ Femoral Dual-Energy X-ray Absorptiometry Related to Ash Weight, Bone Size and Density, and its Relationship with Mechanical Failure Loads of the Proximal Femur", *Osteoporos Int.*, vol. 11, pp. 361-367, Nov 2000

FE-based strength estimation for the prediction of femoral neck fracture

C. Falcinelli², E. Schileo², M. Morawska¹, M. Viceconti^{1,3} and F. Taddei¹

¹ *Laboratorio di Tecnologia Medica, Istituto Ortopedico Rizzoli, Italy*

² *Laboratorio di Bioingegneria Computazionale, Istituto Ortopedico Rizzoli, Italy*

³ *Department of Mechanical Engineering, University of Sheffield, UK*

Abstract— Finite element (FE) models from CT data are a promising tool to non-invasively assess the bone strength and the risk of fracture of bones in vivo in individual patients. They are often used to predict bone strength in a pre-defined and usually simplified loading case. When used to this purpose, they have demonstrated a high accuracy in predicting bone strains and bone strength in vitro and have also been applied in clinical studies, but routine clinical applications have not started since their superiority in clinical predictivity has not been proved yet. The aim of this work is to use validated FE models in order to identify fracture cases within a clinical cohort. The preliminary results showed that FE-based bone strength could be a suitable candidate to discriminate fractured versus non fractured.

Keywords—Bone Strength, Finite Element Analysis, Femoral Fractures, Osteoporosis.

I. INTRODUCTION

Femoral neck risk of fracture is currently estimated starting from areal bone mineral density (aBMD) as measured from DXA (e.g. T-score). This permits only a limited evaluation of fracture mechanical determinants. As a consequence, it shows limitations in identifying cases at risk, even when used in combination with recent indices (e.g. FRAX) incorporating other risk factors (age, life habits, previous fractures) [7].

The use of finite element (FE) models from CT data, that can model the personalised mechanical determinants of fracture, has been often proposed to overcome these limitations. The first applications of FE models in clinical studies have been recently reported [1], [4], [5] but so far they have not shown a neat superiority with respect to BMD. The aim of this work is to assess the ability of an FE modelling procedure - validated for the prediction of strains and the identification of fracture patterns [6] - to identify fracture cases within a clinical cohort.

II. METHODS

The data have been issued by two clinical studies (44 patients, 7 fractured, 37 non-fractured). Each patient underwent a clinical hip CT, from which volumetric femoral neck BMD was measured, and a DXA, from which femoral neck and total hip aBMD were measured.

The FE models (right femur for non-fractured and the remaining intact femur for fractured) were generated starting from CT using an in-vitro validated procedure [6].

Bone strength was evaluated in quasi-axial loading conditions, for a set of 12 different configurations sampling the cone of recorded in vivo hip joint reactions [3]. Bone strength was defined as the minimum load (among the 12 configurations) inducing on the femoral neck surface an

elastic principal strain value greater than a limit value [2].

III. RESULTS AND DISCUSSION

FE predicted femoral strength had a weak correlation with femoral neck and total hip aBMD, and with volumetric BMD. Spearman ρ was respectively 0.6, 0.57 and 0.46, significantly lower than those reported by [4] and [5]. This indicates that the proposed FE prediction is not equivalent to BMD derived indices, while the existing studies concluded for a substantial equivalence of FE-derived and BMD-derived indices in classifying fracture cases.

The mean FE predicted strength of fractured cases was 22% less than that of non-fractured cases. This value is greater than those reported by [4] for women (13% in quasi-axial loading, 18% in side-fall), indicating a good potential of the proposed method to classify fracture cases.

In order to derive an optimal threshold to classify cases at risk, a logistic regression was performed and a ROC curve (Fig. 1) for the discrimination of fractured versus non fractured cases was derived based on the value of the predicted FE strength. An optimal threshold value of 3000N was identified, concordantly to [1]. However, the AUC (Area under curve) was 0.72, lower than that reported in [1]. This lower performance may be related to the two main limitations of the present study: the low number of fractured cases and the absence of side-fall modelling. The number of fracture cases will likely increase in the prosecution of the study. Model validation in side-fall conditions is being established [8] and will soon be included. A further step to improve the model predictivity may be to define a general risk index by considering the whole loading spectrum that a patient may experience.

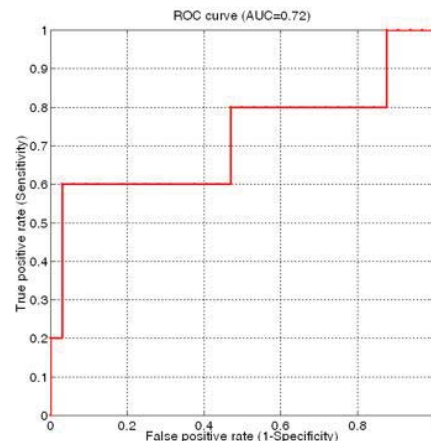


Fig. 1. Receiver operating characteristic (ROC) in order to discriminate fractured versus non fractured cases (AUC=0.72)

ACKNOWLEDGEMENT

EU project VPHOP (FP7-2008-ICT-224635) and Region-University Research Program 2007-2009.

REFERENCES

- [1] Amin *et al.*, "Association of hip strength estimates by finite-element analysis with fractures in women and men", *JBMR*, 26 :1593-1600, 2011.
- [2] Bayraktar *et al.*, "Comparison of the elastic yield properties of human femoral trabecular and cortical bone tissue", *J Biomech*, 37:27-35, 2004.
- [3] G. Bergamann *et al.*, "Hip contact forces and gait patterns from routine activities" *J Biomech*, 34:859-871, 2001.
- [4] Keyak *et al.*, "Comparison of the elastic yield properties of human femoral trabecular and cortical bone tissue", *Bone*, 48 :1239-1245, 2011.
- [5] Orwoll *et al.*, "Finite element analysis of the proximal femur and hip fracture risk in older men", *JBMR*, 24:475-483, 2009.
- [6] E. Schileo, F.Taddei, L.Cristofolini, M. Viceconti, "Subject-specific finite elements models implementing a maximum principal strain criterion are able to estimate failure risk and fracture location on human femurs tested in vitro", *J Biomech*, 41:356-367, 2008.
- [7] Tremolieres *et al.*, "Fracture risk prediction using BMD and clinical risk factors in early postmenopausal women: sensitivity of the WHO FRAX tool", *JBMR*, 25:1002-1009, 2010.
- [8] Grassi *et al.*, "Accuracy of finite element strain predictions in sideways fall configurations for the proximal human femur" doi:10.1016/j.jbiomech.2011.10.019.

Helical flow in carotid bifurcation: influence on exposure to disturbed shear

D. Gallo¹, D.A. Steinman², P.B. Bijary², and U. Morbiducci¹

¹ Department of Mechanical and Aerospace Engineering, Politecnico di Torino (Italy)

² Department of Mechanical & Industrial Engineering, University of Toronto (ON, Canada)

Abstract—Based on hemodynamic simulations data of 50 carotid bifurcations, a linear regression analysis was performed to assess the potential for a combination of helicity-based bulk flow indicators in describing the exposure to disturbed shear. The statistical model revealed a significant relationship with adjusted R^2 values approaching 0.6 ($P < 0.0001$) revealing that a high amount of helicity is instrumental in suppressing flow disturbances. However this protective effect could be moderated when only one direction of rotation is dominant in the flow field. Our findings could have clinical implications, because reliable bulk flow features can be measured in vivo while wall shear stress measurements still suffer from limitations.

Keywords— Atherosclerosis, wall shear stress, helicity, bulk flow.

I. INTRODUCTION

IN the past, it has been observed that atherosclerotic plaques tend to occur where the wall shear stress (WSS) is low and oscillatory (hereafter summarized as “disturbed shear”). Hence, an accurate assessment of the WSS distribution is crucial. However, reliable in vivo WSS derivation is still affected by inaccuracies or uncertainties [1]. To partially overcome limitations from in vivo WSS measurements, image-based computational fluid dynamics (CFD) has allowed, in the last decades, to demonstrate proofs of concept for discovery of relationships among in vivo measurable quantities and exposure to disturbed shear, identifying practical measurable risk factors.

Moreover, there is evidence that helical blood flow (1) elicits atheroprotective fluid-wall interaction processes, by limiting flow instabilities within the cardiovascular bed [2],[3] and (2) regulates the transport of atherogenic particles at the luminal surface [4]. The feasibility of in vivo quantification of helicity has been demonstrated recently [5],[6].

In the present study we aim to determine whether surrogate bulk flow markers of disturbed flow based upon helicity could provide measurable indicators of potential clinical use.

II. METHODS

A. Computational hemodynamics and quantification of disturbed shear

The lumen geometries of 50 ostensibly healthy carotid bifurcations were reconstructed from MRI images [7]. Computational fluid dynamics simulations were carried out for each of the 50 bifurcation geometries. Details on CFD simulations are provided in [7]. The distributions at the vessel wall of relative residence time (RRT) was computed. For a given model, disturbed flow was quantified as the fraction of

the surface area (SA_{rel}) exposed to RRT above a threshold value representing the 80th or 90th percentile of the RRT distribution over the combined surface of all 50 models.

B. Quantification of helicity

By definition, the helicity $H(t)$ of a fluid flow confined to a domain D of three-dimensional Euclidean space \mathbf{R}^3 is given by

$$H(t) = \int_D \mathbf{v}(\mathbf{x},t) \cdot \boldsymbol{\omega}(\mathbf{x},t) dV = \int_D H_k(\mathbf{x},t) dV \quad (1)$$

where $\mathbf{v}(\mathbf{x},t)$ and $\boldsymbol{\omega}(\mathbf{x},t)$ are the velocity and the vorticity vector, respectively, and their internal product H_k is the helicity density. The orientation of the velocity field with respect to the vorticity field is given by the local value of the cosine of the angle between the velocity and vorticity vectors, obtained through the normalization of the helicity density H_k :

$$LNH(\mathbf{x},t) = \frac{\mathbf{v}(\mathbf{x},t) \cdot \boldsymbol{\omega}(\mathbf{x},t)}{\|\mathbf{v}(\mathbf{x},t)\| \|\boldsymbol{\omega}(\mathbf{x},t)\|} \quad (2)$$

This quantity has been proven to be useful for the visualization of complex flow patterns [2], [3], [6].

The 50 carotid bifurcations were characterized in terms of helical content and helical flow topology using Eulerian descriptors. To reach this aim, a quantitative analysis was obtained by applying the descriptors listed in Table I.

C. Statistical analysis

Multivariate linear regression analysis was performed to assess the potential for a combination of helicity descriptors in describing the exposure to disturbed shear. The overall quality of the regression was assessed using Pearson’s correlation coefficient, adjusted by the number of independent predictors (R^2_{adj}). Multivariate linear regression models built from different combinations of helicity-based descriptors underwent a selection based on the minimization of the Akaike information criterion (AIC) [8].

III. RESULTS

A. Relationship between bulk flow features and disturbed shear

The optimal combination of helicity-based descriptors in the multivariate linear regression analysis was selected by AIC (Table II). It was found that: (1) the optimal statistical model of exposure to disturbed flow as identified by AIC is composed by descriptors h_2 and h_4 as independent variables (Table 1); (2) the combination of h_2 and h_4 is a strong predictor of exposure to disturbed flow; (3) the exposure of an individual carotid bifurcation to disturbed shear rises as h_2 decreases and as h_4 increases. Roughly speaking, the

exposure to risk is higher in the presence of low helicity in the bulk flow and when helical flow structures with a preferential rotational direction predominate in the flow field.

Figure 1 shows on the top row the 5 cases with the highest SA_{rel} , in the bottom row the 5 lowest SA_{rel} cases. The same models are shown in Fig. 2, where isosurfaces of LNH averaged over the cardiac cycle are visualized. The correspondence between helical flow arrangement and exposure to disturbed shear is evident, the bottom row cases showing the development of two large counter rotating helical structures.

IV. DISCUSSION AND CONCLUSIONS

From our results it follows that helical flow is an emerging hemodynamic feature in the carotid bifurcation that is common to normal individuals. A high amount of helicity is instrumental in suppressing flow disturbances; however this protective effect can be moderated when one direction of rotation is dominant in the flow field.

In the future, robust prediction of disturbed shear by surrogate markers such as helicity-based bulk flow descriptors might offer a practical way to overcome in vivo WSS measurement limitations, opening opportunities for large scale in vivo studies. Our conviction is enforced by recent proofs of evidence that in vivo quantitative helical blood flow analysis is feasible [5],[6], using phase-contrast MRI. In conclusion, prediction of disturbed shear by robust bulk flow feature analysis may offer a practical way to large-scale in vivo studies of local risk factors in atherosclerosis.

REFERENCES

- [1] L. Boussel, V. Rayz, G. Acevedo-Bolton, M.T. Lawton, R. Higashida, W.S. Smith, W.L. Young, and D. Saloner, "Phase-contrast magnetic resonance imaging measurements in intracranial aneurysms in vivo of flow patterns, velocity fields, and wall shear stress: comparison with computational fluid dynamics", *Magn. Reson. Med.*, vol. 61, pp. 409-417, 2009.
- [2] U. Morbiducci, R. Ponzini, M. Grigioni, and A. Redaelli, "Helical flow as fluid dynamic signature for atherogenesis in aortocoronary bypass. A numeric study", *J Biomech.*, vol. 40, pp. 519-534, 2007.
- [3] U. Morbiducci, R. Ponzini, G. Rizzo, M. Cadioli, A. Esposito, F. De Cobelli, A. Del Maschio, F.M. Montecvecchi, and A. Redaelli, "In vivo quantification of helical blood flow in human aorta by time-resolved three-dimensional cine phase contrast MRI", *Ann. Biomed. Eng.*, vol. 37, pp. 516-531, 2009.
- [4] X. Liu, F. Pu, Y. Fan, X. Deng, D. Li, and S. Li, "A numerical study on the flow of blood and the transport of LDL in the human aorta: the physiological significance of the helical flow in the aortic arch", *Am. J. Physiol. Heart Circ. Physiol.*, vol. 297, pp. H163-H170, 2009.
- [5] A. Harloff, F. Albrecht, J. Spreer, A.F. Stalder, J. Bock, A. Frydrychowicz, J. Schollorn, A. Hetzel, M. Schumacher, J. Hennig, M. Markl, "3D blood flow characteristics in the carotid artery bifurcation assessed by flow-sensitive 4D MRI at 3T", *Magn. Reson. Med.*, vol. 61, pp. 65-74, 2009.
- [6] U. Morbiducci, R. Ponzini, G. Rizzo, M. Cadioli, A. Esposito, F.M. Montecvecchi, and A. Redaelli, "Mechanistic insight into the physiological relevance of helical blood flow in the human aorta. An in vivo study", *Biomech. Model. Mechanobiol.*, vol. 10, pp. 339-355, 2001.
- [7] S.W. Lee, L. Antiga, J.D. Spence, and D.A. Steinman, "Geometry of the carotid bifurcation predicts its exposure to disturbed flow", *Stroke*, vol. 39, pp. 2341-2347, 2008.
- [8] H. Akaike, "A new look at the statistical model identification", *IEEE Trans. Automat. Control*, vol. 19, pp. 716-723, 1974.

TABLE I

HELICITY-BASED BULK FLOW DESCRIPTORS

Descriptor	Definition	Description
h_1	$\frac{1}{V} \int_T \int_V H_k dV dt$	Integral measure of helicity, accounting for changes in sign of H_k .
h_2	$\frac{1}{V} \int_T \int_V H_k dV dt$	Integral measure of the absolute value of H_k : total amount of helicity in the fluid domain.
h_3	$\frac{h_1}{h_2}$	Ranging between -1 and +1 when only left- or right-handed (respectively) helical structures are present in the domain and it equals 0 in case of reflectional symmetry.
h_4	$ h_3 = \frac{ h_1 }{h_2}$	As for h_3 , but neglecting what is the major direction of rotation.
h_5	$\frac{\int_T \int_{V_d} dV_d dt}{\int_T \int_{V_m} dV_m dt}$	Ratio between the volumes occupied by helical rotating structures. The volume occupied by the dominant direction (V_d) of rotation is the numerator, the minor direction of rotation volume (V_m) is the denominator.
h_6	$\frac{\frac{1}{V_d} \int_T \int_{V_d} H_{k,d} dV_d dt}{\frac{1}{V_m} \int_T \int_{V_m} H_{k,m} dV_m dt}$	Ratio between the mean volumetric helicity values over the volume occupied by the dominant and the minor direction of rotation.

T is the cardiac cycle and V is the carotid bifurcation volume.

TABLE II

MULTIVARIATE LINEAR REGRESSION ANALYSIS

	RRT80		RRT90
R^2_{adj}	0.576	R^2_{adj}	0.461
Model	$\{h_2, h_4\}$	Model	$\{h_2, h_4\}$

Best fitting models given by AIC, P -value<0.0001.

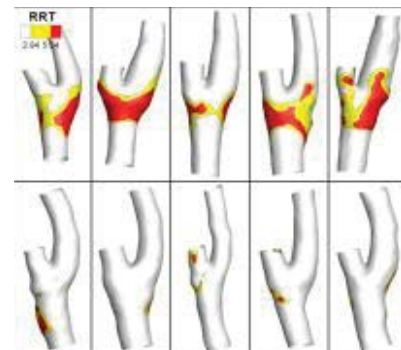


Fig. 1. Exposure to low and oscillatory shear. Bifurcations on the top row have the highest SA_{rel} values and bifurcations in the bottom row have the lowest SA_{rel} values.



Fig. 2. Isosurfaces of LNH averaged over the cardiac cycle on the cases shown in Fig. 1. The different flow arrangement from top to bottom row is evident.

Patient specific multi-scale hemodynamic computational model for planning vascular access surgery in hemodialysis patients

S. Manini¹, L. Antiga^{1,2}, L. Botti³, and A. Remuzzi^{1,3}

¹ *Biomedical Engineering Department, Mario Negri Institute, Bergamo, Italy*

² *Orobix S.r.l, Bergamo, Italy*

³ *Industrial Engineering Department, University of Bergamo, Bergamo, Italy*

Abstract—A number of computational approaches have been proposed for the simulation of hemodynamics and vascular wall dynamics in complex vascular networks. Among them, 0D and 1D pulse wave propagation methods allow to efficiently model flow and pressure distributions and wall displacements throughout vascular networks at low computational costs. Although several techniques are documented in the literature, widely available, open-source computational tools are still lacking. In this work, we present pyNS, a modular solver framework for 0D/1D problems developed in the context of the ARCH (FP7-ICT-2007-2-224390) project and released under a BSD license as part of the archToolkit (<http://archtk.github.com>). pyNS is written in the Python programming language and leverages on the Numpy libraries.

Keywords—Vascular access, hemodialysis, blood flow adaptation, anastomosis, wall shear stress.

I. INTRODUCTION

MORE than 940 patients affected by end-stage renal disease per million population in Europe are on chronic therapy by hemodialysis (HD) (EDTA (2011)) and this number increases annually at a constant rate of about 8%. The Achilles heel of HD is the vascular access (VA) used to connect patient circulation to the artificial kidney. Medical societies and guidelines [1][2] strongly recommend the use of native arteriovenous fistula (AVF), surgically created in the arm with the anastomosis of an artery and a vein. However, short- and long-term VA dysfunctions, including non-maturation (inadequate increase in blood flow volume after surgery), stenosis due to intimal hyperplasia, and ultimately thrombotic occlusion, are the major cause of morbidity and hospitalisation in HD patients, with more than 90,000 procedures/year performed in Europe for revision or reoperation. The extent of this major clinical problem points out the need of prediction and prevention of VA dysfunction. However, to date, they still represent open clinical challenges. A number of computational approaches have been proposed for the simulation of hemodynamics and vascular wall dynamics in complex vascular networks, which could potentially be used to simulate blood flow volume change after VA creation. Among them, 0D and 1D pulse wave propagation methods allow to efficiently model flow and pressure distributions and wall displacements throughout vascular networks at low computational costs. Although

several techniques are documented in the literature, widely available, open-source computational tools are still lacking. During the VPH-I ARCH project, specific computational modelling tools were developed to simulate both pre- and post-operative volumetric blood flow rate, and embedded in an open-source framework (archTk, <http://archtk.github.com>). As an application, we present patient-specific models of the systemic circulation and detailed upper extremity for use in the prediction of maturation after creation of vascular access for hemodialysis [3].

II. METHODS

pyNS has been designed with an object-oriented approach, which allows to abstract the concept of element from the numerical solver itself. The mathematical model implemented in pyNS is based on the work of Hughes and Lubliner [4] by using the 1D Reynolds transport theorem. The relation between pressure p and volumetric flow rate q are derived from conservation of mass and momentum by assuming fully-developed incompressible Newtonian volumetric flow rate in a straight vessel [3]. The convection term, the axial diffusion term and the effect of body forces in the momentum equation are neglected because their contributions are expected to be small [3][5]. An expression for the wall shear stress (WSS) as function of p and q is derived from a time and frequency dependent approximated velocity profile [6], which is based on boundary layer theory. pyNS, on the basis of the momentum equation, represents the vascular network as a graph in which each edge is associated to a mathematical model of pressure (p), volumetric flow rate (q) and wall-shear stress (WSS) in that segment. Arterial and venous segments are modelled using a 1D wave propagation element which consists of a resistor per unit length R (representing the resistance to volumetric flow rate through the vessel) and an impedance per unit length L (representing the inertia of the blood) in series. To incorporate the storage capacity of the vessel in the model, a capacitor C is added to each side of the vascular segment, representing half of the total vascular compliance over that segment. At arterial ends, arteries are terminated with a 0D three-element Windkessel model [2][5] consisting of a characteristic impedance, Z_{wk} , a resistance, R_{wk} and a compliance, C_{wk} .

In addition, a computational 0D model of the anastomosis, i.e. the surgical connection between the feeding artery and the outflow vein, was developed and included in the vascular network. The anastomosis element cannot be modeled using fully developed flow because the radial velocity component is no longer infinitesimally small compared to the axial velocity and flow separation are expected to occur. In order to properly account for non-linear pressure losses anastomosis, 3D computational fluid dynamics (CFD) models were employed in order to estimate pressure drops occurring over the anastomosis for a clinically relevant range of input flow rates and for a variety of anastomosis configurations. The resulting pressure-flow relations (Fig.2) were then lumped as a non-linear resistance in the anastomosis element.

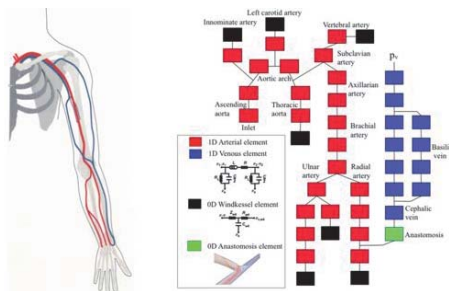


Fig. 1. Vascular network model representing a lower arm radio-cephalic end-to-end fistula. Arterial (red) and venous (blue) segments. The green segment represents end-to-end arteriovenous fistula (AVF) between radial artery and lower cephalic vein.

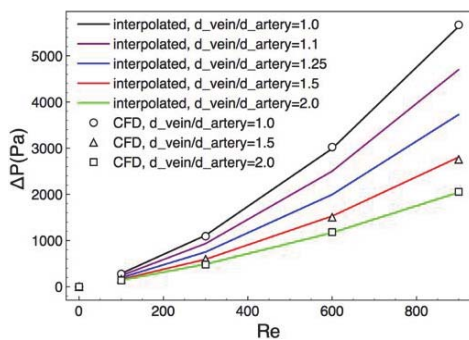


Fig. 2. Pressure drops across the anastomosis.

III. RESULTS

As shown in Fig.3, blood vessel diameters change upon change in blood flow volume induced by AVF shunt. Radial artery diameter and lower cephalic vein diameter increased depending on peak value of WSS. Lower cephalic vein diameter increased more than radial artery diameter due to a lower peak WSS reference value and a lower starting diameter leading to a higher peak WSS value. This behaviour is physiologically correct and expected according to several evidences in literature [7]. Simulating the situation after 40 days from surgery we observed that mean flow volume in the radial artery increases from a preoperative value of 18 mL/min

(Fig.4, left) to 476 mL/min after 40 days from surgery (Fig.4, right).

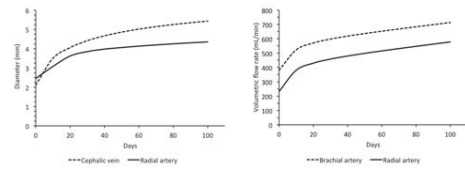


Fig. 3. Radial artery and lower cephalic vein volumetric flow rate (left) and diameter (right) during vascular adaptation induced by AVF shunt.

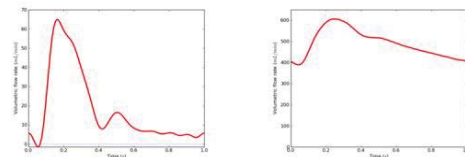


Fig. 4. Radial artery volumetric flow rate before AVF (left) and after 40 days from AVF surgery (right).

IV. CONCLUSION

This computational tool could potentially be used for surgical planning of AVF, to predict VA outcome. Predicting patient-specific blood flow volume increase, resulting from VA creation and vascular adaptation using different AVF configurations, could help the surgeon choosing the most appropriate AVF location (e.g. in case of too low predicted blood flow resulting from a lower arm AVF, a more proximal location should be preferred), ultimately leading to a lower proportion of post-operative VA dysfunctions.

ACKNOWLEDGMENT

The research leading to these results has received funding from the European Communitys Seventh Framework Programme (FP7-ICT-2007-2: Project ARCH n. 224390).

REFERENCES

- [1] J. Tordoir, B. Canaud, P. Haage, K. Konner, A. Basci, D. Fouque, J. Kooman, A. Martin-Malo, L. Pedrini, F. Pizzarelli. *ERA-EDTA; EBPG on vascular access*, 3rd ed. Nephrology Dialysis Transplantation: 22(suppl 2):ii88, 2007.
- [2] National Kidney F. 2006. *Clinical practice guidelines and recommendations 2006 updates*. Kidney Learning System (KLS).
- [3] W. Huberts, A. Bode, W. Kroon, R. Planken, J. Tordoir, F. van de Vosse, E. Bosboom. *A pulse wave propagation model to support decision-making in vascular access planning in the clinic*. Medical Engineering and Physics (in press). 2011. Elsevier.
- [4] T. Hughes and J. Lubliner. *On the one-dimensional theory of blood flow in the large vessels*. Math Biosci, 18(6-7), 61170, 1973.
- [5] P. Reymond, F. Merenda, F. Perren, D. Rufenacht, and N. Stergiopoulos. *Validation of a one-dimensional model of the systemic arterial tree*. Am. J. Physiol. Heart Circ. Physiol., 297(1), H208-22, 2009.
- [6] D. Bessems, M. Rutten, and F. van de Vosse. *A wave propagation model of blood flow in large vessels using an approximate velocity profile function*. J. Fluid Mech., 580, 145-168, 2007.
- [7] K. Konner, B. Nonnast-Daniel, and E. Ritz. *he arteriovenous fistula*. Journal of the American Society of Nephrology 14(6):1996.

Innovative low-cost microgravity bioreactor for hydrogel-based regenerative medicine strategies

D. Massai¹, G. Cerino¹, D. Gallo¹, D. Lorusso¹, C. Ciobanu², U. Morbiducci¹, F.M. Montevecchi¹

¹ Politecnico di Torino, Italy

² Petru Poni Institute of Macromolecular Chemistry, Romania

Abstract—An innovative low-cost perfusion bioreactor was designed for testing and culturing cell-seeded hydrogel microspheres in microgravity condition. Optimal design and culture conditions were identified by a multiscale computational fluid dynamic approach providing a comprehensive investigation of the functioning of the device.

Keywords—Microgravity condition, Suspension, Hydrogels, Bioreactor.

I. INTRODUCTION

IN regenerative medicine, hydrogel-based injectable scaffolds, as cell and bioactive molecule carriers, are becoming a promising strategy for supporting the regeneration of biological tissues [1]. The rationale for this study was to design an innovative low-cost perfusion bioreactor (for which an IPR application is pending, Fig. 1a), dedicated to provide a suitable biochemical and hydrodynamic environment for testing viability, growth and differentiation of cells cultured on hydrogel microspheres in microgravity condition.

The peculiar geometric features of the bioreactor, in conjunction with proper operating conditions, assure the formation of buoyant vortices within the culture chamber. The establishment of this fluid dynamic regime maintains in mixing suspension the microspheres and assures an adequate oxygen transport, guaranteeing microgravity condition without using electromechanical rotating components.

Computational fluid dynamics (CFD) was applied to assist the bioreactor design, by investigating both the effect of the bioreactor geometry on suspension of hydrogel microspheres and the hydrogel-medium interactions, and to identify the operating conditions that optimize mass transport within the culture chamber, providing a comprehensive investigation of the functioning of the device.

II. MATERIALS AND METHODS

The principal components of the bioreactor are: the culture chamber, the check valve system, and the filter (Fig. 1b). The culture chamber (polycarbonate) was designed with a particular geometry for inducing the detachment of the fluid vein from the walls and the consequent formation of medium mixing slow vortexes within the chamber. The check valve system (AISI 316L), provided with a holed membrane (silicone) that moves according to the pressure gradients, was designed for guarantying the unidirectionality of the flow. The filter (AISI 316L), located within the culture chamber, was designed in order to prevent accidental outputs of microspheres during the recirculation of the culture medium. In detail, the culture medium enters from the base of the

bioreactor, moves through the check valve, pervades the culture chamber, and flows out from the top (Fig. 1b).

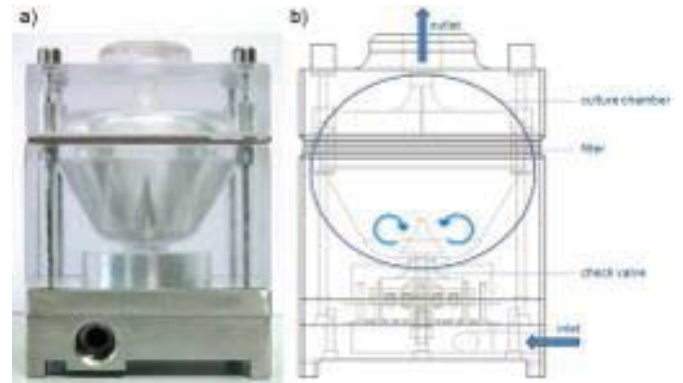


Fig. 1. a) Bioreactor (95 mm x 70 mm x 70 mm; priming volume = 50 ml); b) Bioreactor constructive drawing with detailed components.

For assisting the bioreactor design and to identify the proper operating conditions, multiphase axial symmetric CFD simulations were performed, by adopting a finite volume method (Fluent 6.3.26, ANSYS Inc.). For the mesh generation, the solid modeler Gambit (ANSYS Inc.) was used. The culture medium was simulated as a Newtonian fluid (density=1006.5 kg/m³, viscosity = 0.001 kg/(m·s)), and the physically crosslinked polyurethane hydrogel microspheres (density = 1118 kg/m³) were modelled with a diameter of 500 μm.

The CFD simulations were carried out varying the inlet velocity of the culture medium, in order to guarantee Reynolds numbers lower than 1000 at inlet section (laminar flow condition). Both the phases, culture medium (primary fluid phase of mixture) and hydrogels (secondary phase), are present simultaneously, and were modelled using the Eulerian-Eulerian multiphase model. At the wall, no slip-conditions were imposed.

Preliminary operating tests were conducted using distilled water as culture medium, and physically crosslinked polyurethane hydrogel microspheres (by Petru Poni Institute). The perfusion system is composed of a peristaltic pump, media reservoir, oxygen-permeable tubes, and quick-disconnect couplings (Fig. 2).

III. RESULTS AND DISCUSSION

Findings from computational simulations allowed to optimize the bioreactor geometry, and to identify the operating conditions for the preliminary operating tests (flow rate range = 20-30 ml/min).



Fig. 2. Set up of the perfusion system of the bioreactor, adopted for the preliminary operating tests, and composed of peristaltic pump, media reservoir, oxygen-permeable tubes, and quick-disconnect couplings.

In accordance with the computational results (Fig. 3a), experimental tests (Fig. 3b) demonstrated the suitability of the bioreactor geometry: the proper combination of the fluid dynamic conditions establishing within the chamber, and the shape of the side walls of the chamber give rise to flow separation, with the consequent formation of stationary buoyant vortices and of hydrodynamic forces within the culture chamber.

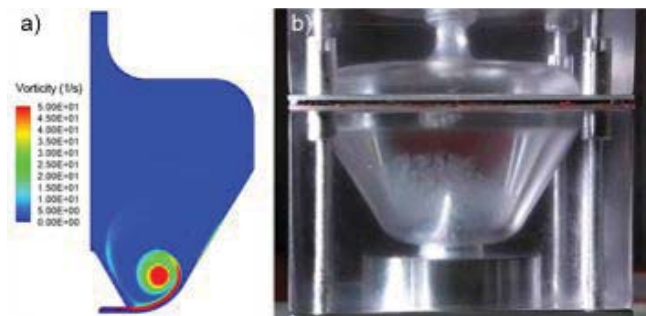


Fig. 3. a) Colour maps of culture medium vorticity magnitude values; b) Suspended hydrogel microspheres within the bioreactor.

The balance between hydrodynamic and gravitational forces within the culture chamber guarantees the establishment of microgravity condition, that allows (1) to maintain microspheres in homogeneous suspension, (2) to provide suitable mass transfer and oxygen transport, and (3) to avoid both the sedimentation of microspheres at the bottom of the chamber, and their crushing on the filter.

Moreover, computational simulations allowed to verify that the generated microgravity condition [2] avoids shear stress values critical for the cells (maximum shear stress = 0.4 Pa), conversely to what has been reported for dynamic bioreactors based on the agitation/stirring mechanism, where the onset of turbulences in the fluid flow typically occurs [3].

IV. CONCLUSION

The present study describe an innovative low-cost perfusion bioreactor for cell-seeded hydrogel culture, that allows to maintain hydrogel microspheres homogeneously suspended in microgravity condition, with a suitable mass transfer and oxygen transport, avoiding critical shear stresses for the cells, and without incorporating rotating components.

In the near future, experimental tests with cell-seeded hydrogel microspheres will be performed.

ACKNOWLEDGEMENT

The present work was carried out in the scope of BIOSCENT Project (ID 214539).

REFERENCES

- [1] Li Z. and Guan J., *Hydrogels for Cardiac Tissue Engineering*, *Polymers*, 3:740-761, 2011.
- [2] Gerecht-Nir S., Cohen S., Itskovitz-Eldor J., *Bioreactor Cultivation Enhances the Efficiency of Human Embryoid Body (Heb) Formation and Differentiation*, *Biotechnol. Bioeng.*, 86:493-502, 2004.
- [3] King J. and Miller W.M., *Bioreactor Development for Stem Cell Expansion and Controlled Differentiation*, *Curr. Opin. Chem. Biol.*, 11:394-398, 2007.

Analytical wear model of hip implants

L. Mattei¹ and F. Di Puccio¹

¹ *Department of Mechanical, Nuclear and Production Engineering, University of Pisa, IT*

Abstract—Although hip arthroplasty is considered one of the most successful orthopedic surgeries, the tribological performance of hip implants remains a critical issue and wear is recognized as the main cause of their failures. Recently many theoretical studies have been addressed to implant preclinical wear evaluation, mainly based on Finite Element simulations. This study presents a mathematical wear predictive model of hip prostheses, developed in Mathematica®, suitable for metal-on-plastic and metal-on-metal replacements. The model has been used to investigate the effect of implant design, i.e. geometry and materials, and operating conditions on wear.

Keywords—Wear prediction, Hip implants, Cross-shear, Friction

I. INTRODUCTION

THE wear of hip implant surfaces is nowadays recognized as the main cause of their failure. In the most widespread soft-on-hard (SoH) implants, the low wear resistance of the plastic cup determines a production of wear debris that can induce an adverse response of tissues causing osteolysis and implant loosening. Although hard-on-hard (HoH) implants show lower wear rates than SoH ones, they can release toxic metal ions as a consequence of wear damage. These drawbacks have made preclinical wear evaluation extremely important for hip implants. To this aim in the last decade many wear models have been proposed, as reviewed in [1], rarely for metal-on-metal (MoM) implants [4] whilst mainly for metal-on-plastic (MoP) coupling [2]-[3], describing the cross-shear (CS_s) effect of UHMWPE. The objective of our research is to investigate the wear both of SoH and HoH implants by means of a mathematical wear model able to simulate long-term wear in physiological conditions. In particular the model has been used to compare several recent wear laws proposed for UHMWPE [5] and to investigate the effect of the boundary conditions [5]-[6] and friction on wear.

II. MATERIAL AND METHODS

An analytical and parametric wear predictive model was developed using Mathematica®. The model was formulated for the left hip implant represented in Fig. 1-a.

A. Wear model

The wear model is based on the Archard's wear law since, according to the literature, adhesion and abrasion are the main wear mechanisms involved both in SoH and HoH hip implants. In our model the instantaneous version of the law was conveniently used. It describes the linear wear rate $h_r(P, t)$ at a point P of the worn surface at a time t being

proportional, through a wear factor $k_f(P, t)$, to the product of the contact pressure $p(P, t)$ and the sliding velocity $v(P, t)$

$$h_r(P, t) = k_f(P, t) p(P, t) |v(P, t)| \quad (1)$$

The evaluation of Eq. 1 requires both kinematic and contact analyses, the latter including the identification of the theoretical contact point P_c (Fig. 1-c). Recently a new wear law has been proposed for UHMWPE, stating that the linear wear rate is independent from the contact pressure [3], that is

$$h_r(P, t) = k_c(P, t) |v(P, t)| \quad (2)$$

where k_c is the so-called wear coefficient. Two different versions of the model were developed for SoH and HoH implants, whose characteristics are described below:

1) *Soft-on-Hard*: only the cup is subjected to wear; a frictionless contact is assumed being $f \leq 0.06$ (P_c aligned with the loading direction); $p(P, t)$ calculated by FE simulations; implementation of the most recent wear factors/laws: constant k_f , $k_f(R_a)$ where R_a is the head roughness, $k_f = k_f(CS_s)$, $k_f = k_f(CS_s, \bar{p})$ [2], $k_c = k_c(CS_s)$ [3] (with $CS_s = CS_s(P)$, $\bar{p}(P)$ is the average pressure in a cycle at point P).

2) *Hard-on-Hard*: wear predictions both of cup and head; simulation of the running-in wear (constant k_f); simulation of a rough contact ($f=0.2$) (P_c shifted from the loading direction of the friction angle); $p(P, t)$ according to the Hertzian theory.

As simulation results, the model provides for each component the linear wear depth $h(P)$ and volumetric wear V over a single gait cycle. As the geometrical modifications due to wear were not implemented, the wear after n gait cycles was obtained simply by multiplying h and V by n .

B. Simulated conditions

Wear predictions were performed for a MoP and a MoM hip implant with the following characteristics: $r_h=14$ mm, $cl=0.08$ mm, $\alpha=0^\circ$, $\beta=45^\circ$, $E_p=0.5$ GPa and $\nu_p=0.4$ for UHMWPE, $E_m=210$ GPa and $\nu_p=0.3$ for CoCr.

Physiological 3D walking conditions were assumed, [5].

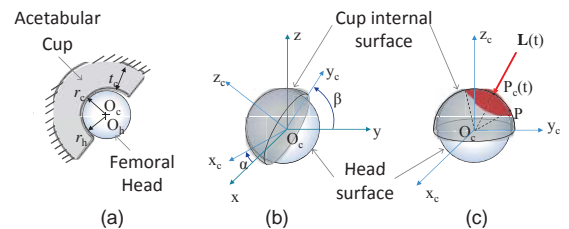


Fig. 1. Geometrical features of the model (a). Reference frames used for model implementation (b). Theoretical contact point (P_c) and contact area (red)(c).

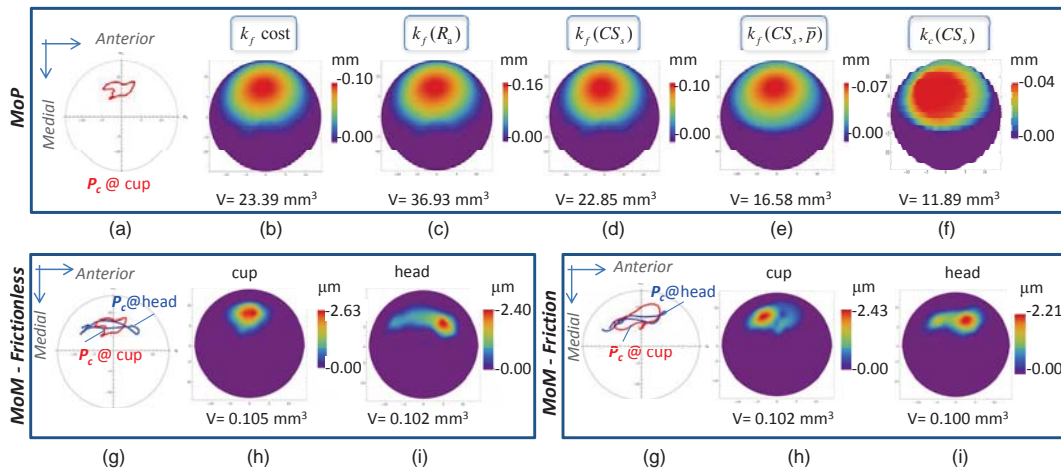


Fig. 2. Main results projected into the $x_c - y_c$ plane: wear predictions for a MoP implant (top) and for a MoM implant (bottom) assuming frictionless (left) and friction contact (right).

III. RESULTS AND DISCUSSION

1) *SoH hip implants*: The trajectory of the theoretical contact point P_c on the acetabular cup is depicted in Fig. 2-a: it is located laterally to the north pole and extended to the anterior and the posterior quadrants. In correspondence of such trajectory, the maximum contact pressure was observed and consequently also the maximum wear depth. The linear wear maps predicted by the proposed model according to different wear laws are shown in Figs. 2-b,f. A qualitative analysis of Figs. 2-b,f points out that similar wear maps are predicted by the models based on the Archard's wear law but differing in the wear factor expression, whilst a different wear distribution was obtained using the new wear law (Eq. 2). Indeed in the latter case, the maximum linear wear affected a wider area. On the other hand, significant differences arise from a quantitative examination of results shown in Fig. 2-b,f: both the linear and the volumetric wear are strongly affected by the particular wear factor/coefficient used. The resulting maximum wear depth and the volumetric wear varied in wide ranges, 0.035–0.158 mm and 12–37 mm³ respectively.

As a general trend, the highest wear was predicted by $k_f(R_a)$; similar wear rates were obtained for constant k_f and $k_f(CS_s)$, whilst the lowest wear rates were for $k_f(CS_s, \bar{p})$ and $k_c(CS_s)$. In terms of relative variations, the wear model based on the $k_f(CS_s)$ resulted the most sensitive to the kinematic and loading conditions. Other simulations detailed in [5] demonstrated that CS_s is a fundamental aspect of UHMWPE wear which needs to be modelled. In particular, it was observed that the more complicated the kinematic conditions, the higher the CS_s and the wear factor/coefficient, the higher the wear indicators. According to our results the kinematics conditions strongly affect wear predictions whilst the loading conditions have a minor the effect.

2) *MoM hip implants*: The results obtained for the MoM implant under frictionless and friction conditions are reported at the bottom of Fig. 2. Both for cup and head the trajectory of P_c and wear indicators were calculated. As for the MoP implant, P_c is located in lateral direction and its trajectory

appears almost circular on the cup and more stretched on the head (Fig. 2-g). This was in agreement with the wear maps: the cup worn area is almost circular (Fig. 2-h), whilst the head ones has a semi-circular shape and covers widely both the posterior and the anterior quadrant (Fig. 2-h). Both the maximum wear depth and the volumetric wear were slightly higher in the cup. The introduction of a rough contact caused wider and more curved trajectories of P_c both on cup and head (Fig. 2-l). Being the contact areas more extended compared to the frictionless case, the wear was redistributed and both the maximum linear wear and the volumetric wear resulted lower (e.g. 2.43 vs 2.64 μm and 0.102 vs 0.105 m³ for the cup). Consequently the simulation of the friction contact, which is an innovative aspect with respect to the literature [4], was demonstrated to have a significant effect on the predicted wear rates.

It is worth noting that, geometry and BCs being the same, the wear of MoM implants was at least two orders of magnitude lower than MoP ones, in agreement with the literature. Moreover, the worn area of the plastic cup is significantly wider than the metal one, because of the higher elastic deformations.

REFERENCES

- [1] L. Mattei, F. Di Puccio, E. Ciulli and B. Piccigallo, *Lubrication and wear modelling of artificial hip joints: a review*, Tribol. Int., 44:532549, 2011.
- [2] L. Kang, A.L. Galvin, J. Fisher and J. Zhongmin, *Enhanced computational prediction of polyethylene wear in hip joints by incorporating cross-shear and contact pressure in addition to load and sliding distance: Effect of head diameter*, J. Biomech., 42:912-8, 2009.
- [3] F. Liu, A.L. Galvin, J. Zhongmin and J. Fisher, *A new formulation for the prediction of polyethylene wear in artificial hip joints*, Proc. IMechE Part H, J. Eng.&Med., 225:1624, 2011.
- [4] M.N. Harun, F.C. Wang, J. Zhongmin and J. Fisher, *Long-term contact-coupled wear prediction for metal-on-metal total hip joint replacement*, Proc. IMechE Part H, J. Eng.&Med., 223:993-1001, 2009.
- [5] L. Mattei, F. Di Puccio, and E. Ciulli, *A comparative study on wear laws for soft-on-hard hip implants using a mathematical wear model*, Tribol. Int., j.triboint.2012.03.002, 2012.
- [6] L. Mattei, F. Di Puccio, and E. Ciulli, *Wear simulation of metal on metal hip replacements: an analytical approach*, Proceed. ESDA 2012, 1-10, 2012 (Accepted).

Two-photon polymerization for engineering stem cell niches

Michele Nava¹, Matteo Laganà¹, Manuela T. Raimondi¹, Veronica Aprile¹, Shane M. Eaton², Giulio Cerullo² and Roberto Osellame²

¹LaBS, Department of Structural Engineering, Politecnico di Milano, Milano, Italy

²IFN-CNR, Department of Physics - Politecnico di Milano, Milano, Italy

Abstract— Recent studies have shown that mechanical factors can direct stem cell fate *in vitro*, even in the absence of biochemical factors. Two-photon laser polymerization was used here to fabricate ultra-precise 3D micro-niches with different architectures and pore size able to structurally interact with cells at the single-cell scale. Our experiments have shown that mesenchymal stem cells, randomly seeded, systematically, colonise the internal volumes of 3D micro-niches and proliferate, while showing a roundish morphology. Even if stem cell mechanobiology is a very complex field, this study shows how mechanical interactions studied in a 3D micro-architecture at a single cell scale may influence stem cells response.

Keywords- Two-photon, polymerization, engineered niche, mesenchymal stem cell

I. INTRODUCTION

AN important challenge for successful translation of new stem cell-based therapy to the clinics consists in gaining a precise control over stem cell differentiation. Stem cell response is controlled by a variety of cues in the native niche e.g. systemic factors, soluble and cell-bound cytokines, cell-extracellular matrix interactions, cell-cell interactions and mechanical factors [1],[2]. Recent studies have shown that mechanical factors e.g. the stiffness of the substrate [3], [4], [5], [6] and the nano-topography of the adhesion surface [7],[8],[9] are able to direct stem cell fate *in vitro*, even in the absence of biochemical factors [10], [11], [12], [13] [5]. Besides these works mainly referred to a 2D approach, there is an increasing interest in the development of 3D synthetic niches [14] that can mechanically interact with adhering cells at a single-cell scale in order to mimic the native niche behavior. A novel technology for fabricating ultra-precise structures controlled at the cell scale (5-10 μm) is two-photon laser polymerization (2PP) [15]. This rapid-prototyping technology allows to fabricate polymeric structures of arbitrary 3D geometry with a spatial resolution down to 100 nm. In this work, we report on the effects of micro-architectural parameters of the scaffold fabricated by 2PP on specific aspects of cell response in 3D culture.

II. MATERIALS AND METHODS

We used MG63 human osteosarcoma to evaluate cell adhesion and morphological compatibility to the 2PP-engineered niches. Furthermore, to study cell viability, adhesion, migration and proliferation within these micro-scaffolds, we used mesenchymal stem cells (MSCs).

We have designed and fabricated by 2PP a series of polymeric niches by varying their 3D geometrical parameters. The niches were straight prismatic structures formed by an external confinement grid made of horizontal

parallel beams, identically spaced by 5 μm in all niche types, and an internal 3D grid of variable geometry and size. The polymerized lines have an elliptical cross section, of approximately 1 μm and 3 μm transverse and vertical dimensions, respectively. Thus, the external walls provided an approximate 2 μm gap between horizontal lines, which allow cell nutrients to pass through while confining cells that scaled the external walls to invade the internal structure of the niche. To test the influence of niche height, we developed two height-types: 20 μm , and 80 to 100 μm ; for each micro-scaffold we developed 4 different internal grids, of fixed pore dimension 10, 20, and 30 μm , or of pore dimension graded from 10 to 30 μm in the horizontal plane (Fig 1).

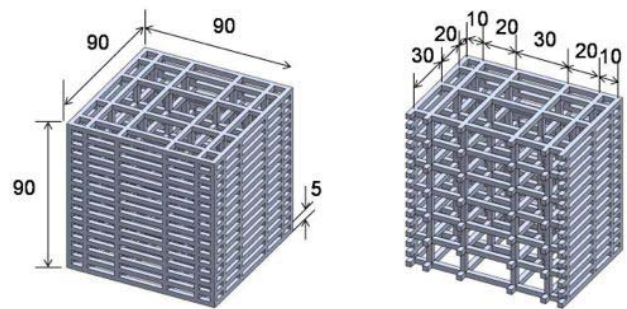


Fig. 1 Schematic of the generic niche architecture engineered by 2PP in axonometry (left) and in frontal section (right). We studied 8 niche types, formed by an external containment grid made of horizontal parallel beams, identically spaced by 5 μm in all niche types, and by an internal 3D pore of variable geometry and size. Dimensions are in microns.

The 2PP-engineered niches were written on a chambered 160- μm thick cover glass (Labtek II, Nunc) with a Ti:Sapphire oscillator (800-nm wavelength, 87-MHz repetition rate, 40-fs pulse duration). Pulses were focused in the photoresist (SZ2080 [16]) with a 1.4-NA microscope objective. The niches were defined using piezoelectric stages (Nanocube, PI) with 100- μm travel range along all three axes. The scan speed and laser power were optimized for the best mechanical integrity of the niches. In the first writing step, the lattice was formed (average power 15 mW) with speeds of 60 $\mu\text{m}/\text{s}$ for 10- μm pore size, 10 $\mu\text{m}/\text{s}$ for the graded pores, and 2 $\mu\text{m}/\text{s}$ for 20 and 30- μm pore sizes. Slower speeds were needed for the larger pore lattices to form stronger lines to compensate for the fewer support beams present. In a second step, the lattice was surrounded by the wall shown in Fig. 1, using a speed of 2 $\mu\text{m}/\text{s}$.

The cells were cultivated for 6 days in static conditions, changing the culture medium every day. One cell-seeded niche was transferred to the ambient chamber of a confocal microscope immediately after cell seeding, and images of the 30x20 niches were acquired in live time-lapse phase contrast, every 5 minutes for 6 days. For viability assessment, cells

were marked in the wells using a Live/Dead viability/cytotoxicity kit. For confocal microscopy, the cell nuclei were marked in blue using Dapi, the cytoskeletal actin was marked in green using FITC-conjugated phalloidin. Cell proliferation was studied by detection of the Ki67 antigen using an anti-Ki67 antibody Cy3 (red)-conjugated. The cell number at 6 culture days was counted on the fluorescence images of the Dapi (blue) and the Ki67 (red) channels.

III. RESULTS

Optimal cell adhesion to the glass bottom of the culture chamber, to the niches external walls and interior lattice was observed both for the MG63 cells and the MSCs (Fig. 2a). For both cell types, we observed a flat morphology in the cells of the monolayer and a more roundish morphology in the cells adhered to the niche walls and particularly in the niche internal volume (Fig. 2a,b,e,f), where the cytoplasmic protrusions anchoring the cells to the beams of the niche were oriented in all spatial directions. By time-lapse phase contrast imaging (Fig. 2c), we observed that, after random cell seeding in suspension, MSCs initially adhered to the glass bottom of the culture chamber in few hours, and then systematically migrated towards the niches, climbed the niche external walls and invaded the niche internal volumes while establishing cell colonies already well discernible at day 4. Such a homing behavior of MSCs occurred in conjunction with all the niche types, except that colonies were not established in the niches with the smallest pore dimension ($10\ \mu\text{m}$), which we attribute to a dimensional incompatibility. The mean cell density in the niches varied significantly among niche types, from a minimum of 2 cells/niche for the 10×100 niche (tall, smallest pore), to a maximum of 22 cells/niche for the $10\text{-}30\times 20$ niche (short, graded pore). With regard to proliferation, we observed a high rate in the central areas of all the MSC monolayer colonies (Fig. 2a,b). Proliferating cells were present also in the niche internal volumes and on the niche external walls (Fig. 2b). The greatest number of proliferating cells was observed in the $10\text{-}30\times 20$ niches.

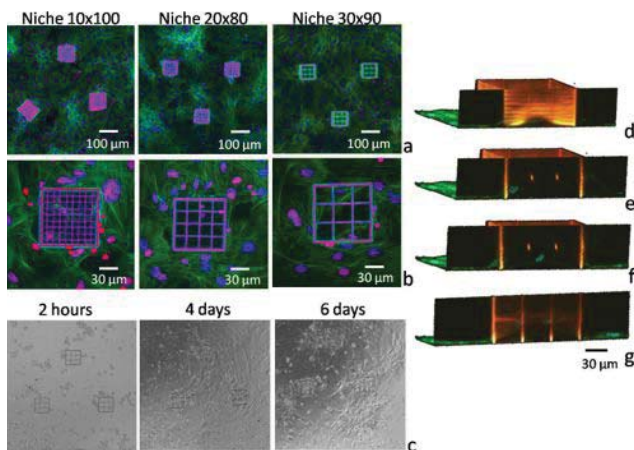


Fig. 2 a) Z-stack projections of low magnification (15 \times) and b) high magnification (60 \times) confocal fluorescence images acquired from MSC-seeded 2PP-engineered niches at 6 culture days. Actin filaments are stained with phalloidin FITC (green). Dividing cells are visualized here by Anti-Ki67 Cy3 (red). Nuclei are counterstained with Dapi (blue). Nuclei of dividing cells co-express Ki-67 and Dapi and appear pink. c) MSCs imaged in phase contrast to document their migration into the 30×20 niches. The 3D rendering (60 \times) visualizes the niche on subsequent parallel frontal sections located (d) at the frontal wall, (e)-(f) at intermediate sections, and (g) near the posterior wall

IV. CONCLUSION

Our aim was to investigate how the 3D micro-architecture of the scaffold influences cell function. Using 2PP fabrication technique, we showed that the adhesion, morphology and proliferation of rat MSCs can be influenced by the geometry. With the exception of niches with the smallest pore dimension ($10\ \mu\text{m}$), cells seeded randomly and systematically migrated toward the micro-niches, demonstrating that the cell scale dimensions of the 3D micro-structures provide a proper micro-environment to cells. We found high proliferation in MSC monolayer colonies with large, spreading cells. Our results are innovative with respect to 2D observations [17], [18]: considering the internal niche volumes, proliferating cells in the scaffold pores assumed a roundish morphology. Even though we are still far away from an engineered stem cell niche, we demonstrated that 3D micro-scaffolds can be realistic representations of a biophysical micro-environment thus can be used to investigate stem cell response in 3D

ACKNOWLEDGEMENTS

This project is funded by: Politecnico di Milano, under grant "5 per Mille Junior 2009 CUPD41J10000490001", by the Italian Institute of Technology (IIT-Genoa), under grant "Biosensors and Artificial Bio-systems", and by the Cariplo Foundation (Milano), under grant 2010 "3D Micro structuring and Functionalisation of Polymeric Materials for Scaffolds in Regenerative Medicine".

REFERENCES

- [1] Silver FH (2006) *Mechanosensing and Mechanochemical Transduction in Extracellular matrix*. Springer. ISBN-10: 0-387-25631-8
- [2] Noda M (2011) Ed. *Mechanosensing biology*. Springer. ISBN 978-4-431-89756-9
- [3] Engler AJ, Sen S, Sweeney HL, Discher DE (2006) Matrix stiffness directs stem cell lineage specification. *Cell* 126(4):677-89
- [4] Legant WR et al. (2010) Measurement of mechanical tractions exerted by cells in three-dimensional matrices. *Nat Methods* 7(12):969-71
- [5] Reilly GC and Engler AJ (2010) Intrinsic extracellular matrix properties regulate stem cell differentiation. *J Biomech* 43:55-62
- [6] Tse JR, Engler AJ (2011) Stiffness gradients mimicking in vivo tissue variation regulate mesenchymal stem cell fate. *PLoS One* 6(1):e15978
- [7] Biggs MJ, Richards RG, Dalby MJ (2010) Nanotopographical modification: a regulator of cellular function through focal adhesions. *Nanomedicine*. 6(5):619-33
- [8] Fu J, Wang YK, Yang MT et al. (2010) Mechanical regulation of cell function with geometrically modulated elastomeric substrates. *Nat Methods* 7(9):733-6
- [9] Nie Z and Kumacheva E (2008) Patterning surfaces with functional polymers. *Nat Mater* 7(4):277-90
- [10] Castillo AB, Jacobs CR (2010) Mesenchymal stem cell mechanobiology. *Curr Osteoporos Rep*. 8(2):98-104
- [11] Huang AH, Farrell MJ, Mauck RL (2010a) Mechanics and mechanobiology of mesenchymal stem cell-based engineered cartilage. *J Biomech* 43(1):128-36
- [12] Huang Y, Jia X, Bai K, Gong X, Fan Y (2010b) Effect of fluid shear stress on cardiomyogenic differentiation of rat bone marrow mesenchymal stem cells. *Arch Med Res* 41(7):497-505
- [13] Lee DA, Knight MM, Campbell JJ, Bader DL (2011) Stem cell mechanobiology. *J Cell Biochem* 112(1):1-9
- [14] Kraehenbuehl TP, Langer R, Ferreira LS. (2011) Three-dimensional biomaterials for the study of human pluripotent stem cells. *Nat Methods* 8(9):731-736.
- [15] Park S (2009) Two-photon stereolithography for realizing ultraprecise three-dimensional nano/microdevices. *Laser & Photon. Rev.* 3:1-11
- [16] Farsari M, Chichkov B (2009) Materials processing: two-photon Fabrication. *Nat. Photonics* 3: 450-52.
- [17] Wan LQ, Kang SM, Eng G et al. (2010) Geometric control of human stem cell morphology and differentiation. *Integr Biol* ;2(7-8):346-53.
- [18] S. A. Ruiz and C. S. Chen, *Stem Cells*, 2008, 26, 2921-2927.

Orbital stability analysis of gait: model and experimental analysis comparison

F. Riva¹, M.C. Bisi¹, L. Cristofolini^{2,3}, and R. Stagni^{1,3}

¹ DEIS, Department of Electronics, Computer Sciences and Systems, University of Bologna, Italy

² DIEM, Department of Mechanical, Nuclear, Aviation and Metallurgical Engineering, University of Bologna, Italy

³ Health Sciences and Technologies – Interdepartmental Center for Industrial Research (HST – ICIR)

Abstract— The understanding of locomotor stability is a critical issue in clinical fall risk assessment procedures. At this purpose, orbital stability analysis is gaining much interest, but still its relationship with fall risk is deemed to be controversial. A possible cause of this controversy lies in the fact that the influence of experimental characteristics on the results has not been investigated yet. To this end, simulations represent a useful tool. The aim of this study was to compare orbital stability results from acceleration data of a stable 5-link walking model to experimental results.

Keywords— Orbital stability, Walking, Fall risk, Floquet multipliers.

I. INTRODUCTION

FALLS in the elderly represent a major community and public health problem, with large clinical and economic consequences [1], [2]. The understanding of locomotor stability is a critical issue in clinical assessment procedures [3]. Many stability indices are present in literature [4], but still there is no commonly accepted way to define or quantify locomotor stability [5]. Some authors in literature proposed the use of nonlinear techniques, like orbital stability analysis, to assess stability of human locomotion [3], [5]. Fundamental indicators of orbital stability are maximum Floquet multipliers (maxFM) quantifying, discretely from one cycle to the next, the tendency of the system's states to return to the periodic limit cycle orbit after small perturbations. If maxFM have magnitude < 1 , perturbations tend to shrink by the next repetition, and the system remains stable [5]. Nevertheless, the use of this technique in the assessment of fall risk has been deemed controversial [4]. A possible cause of this controversy could lie in the fact that still the influence of experimental characteristics on the results have not been investigated. Simulations represent a powerful tool to test reliability of results, and the analysis of a walking model can give precise insights on what the real orbital stability conditions of human walking are. The aim of this study was to compare orbital stability

results coming from acceleration data of a stable 5-link walking model to experimental results.

II. METHODS

A. Model analysis

A 2-dimensional, 5-link stable biped walking model was implemented [6]. The model consisted in one trunk, two thigh and two shank segments. The model orientation was described by stance and swing knee angles, stance and swing hip angles and upper body angle ($\phi_{k,sw}$, $\phi_{k,st}$, $\phi_{h,st}$, $\phi_{h,sw}$, ϕ_{ub} , all with respect to gravity). Anterior-posterior (AP) and vertical (VT) accelerations of the trunk at the level of the fifth lumbar vertebra (L5) were calculated; orbital stability analysis was performed on a 2-dimensional state space composed by the two accelerations. Realistic experimental noise was simulated, and noise-affected acceleration signals were also analysed. Stride cycles were considered as the time between each right heel strike and were resampled to be 100 samples long. Mean values of maxFM across the gait cycle were calculated on increasing number of strides (from 10 to 300).

B. Experimental analysis

10 healthy young participants performed an overground walking task at their preferred speed on a 250m long road with two synchronized inertial sensors (Opal, APDM, Portland, OR, USA) placed at the level of L5 and of the right shank. Right heel strike instants were estimated from the angular velocity of the lower limb with a method based on wavelet analysis [7]. Orbital stability was then calculated on experimental data, based on the same state space used for the model analysis (VT and AP accelerations). Subjects gave informed consent before participating. As for model analysis, stride cycles were considered as the time between each right heel strike and were resampled to be 100 samples long, and mean values of

maxFM across the gait cycle were calculated on increasing number of strides (from 10 to 300) for both state spaces.

III. RESULTS

A. Model results

For less than 30 cycles, values of maxFM calculated on the state space composed by noise free signals gradually decrease (Fig. 1), starting from values near (or above) one. These values indicate very poor stability. Nevertheless, the model is stable, so these values are not to be considered as reliable. From about 30 cycles on, values of maxFM stabilize around the value of 0.34, with a standard deviation of about 0.09.

Results coming from the analysis of noisy accelerations signals are very similar to the ones obtained from noise-free signals; still the value of maxFM tend to stabilize around 0.34 from about 30 cycles on, with a similar trend.

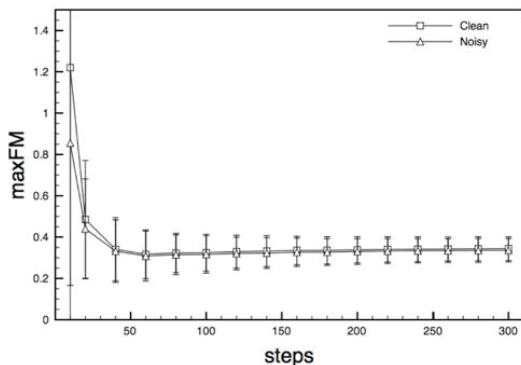


Fig. 1. Mean maxFM values across the stride cycle calculated on state spaces composed by VT and AP accelerations of L5 (noisy and clean) coming from the model for increasing number of stride cycles used in the calculations.

B. Experimental results

MaxFM calculated on experimental accelerations state spaces showed decreasing value for increasing number of cycles analysed (Fig. 2), reaching values close to 0.4 from 80 cycles on, with a standard deviation of about 0.1.

IV. DISCUSSION

Analysis of noisy accelerations state spaces led basically to the same results obtained for the analysis conducted on clean signals; simulated inertial sensor experimental noise did not influence

the maxFM calculation. This can lead to the conclusion that orbital stability analysis performed on state spaces composed by accelerations coming from inertial sensors is robust to noise.

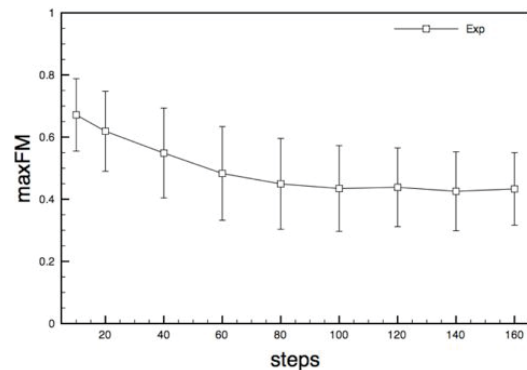


Fig. 2. Mean maxFM values across the stride cycle calculated on state spaces composed by VT and AP accelerations of L5 coming from experimental trials for increasing number of stride cycles used in the calculations.

Experimental results showed slightly higher values for maxFM compared to the model analysis, yet confirming the overall trend. The number of stride cycles needed to reach a reliable value was higher in experimental analysis than in model analysis. Nevertheless, maxFM values confirm that the gait is stable. Experimental walking trial for orbital stability measures should then take into account for no less than 80 stride cycles.

ACKNOWLEDGEMENT

The authors thank Dr. Martijn Wisse for its contribution in the implementation of the model.

REFERENCES

- [1] G. F. Fuller, "Falls in the elderly," *Am Fam Physician*, vol. 61, pp. 2159–2168, 2173–2174, Apr. 2000.
- [2] S. Heinrich, K. Rapp, U. Rissmann, C. Becker, and H.-H. König, "Cost of falls in old age: a systematic review," *Osteoporosis Int*, vol. 21, pp. 891–902, Nov. 2009.
- [3] Y. Hurmuzlu and C. Basdogan, "On the measurement of dynamic stability of human locomotion," *J Biomech Eng*, vol. 116, pp. 30–36, Feb. 1994.
- [4] D. Hamacher, N. B. Singh, J. H. Van Dieën, M. O. Heller, and W. R. Taylor, "Kinematic measures for assessing gait stability in elderly individuals: a systematic review," *J R Soc Interface*, vol. 8, pp. 1682–1698, Dec. 2011.
- [5] J. B. Dingwell and H. G. Kang, "Differences between local and orbital dynamic stability during human walking," *J Biomech Eng*, vol. 129, pp. 586–593, Aug. 2007.
- [6] J. H. Solomon, M. Wisse, and M. J. Hartmann, "Fully interconnected, linear control for limit cycle walking," *Adapt Behav*, vol. 18, pp. 492–506, Dec. 2010.
- [7] K. Aminian, B. Najafi, C. Büla, P.-F. Leyvraz, and P. Robert, "Spatio-temporal parameters of gait measured by an ambulatory system using miniature gyroscopes," *J Biomech*, vol. 35, pp. 689–699, May 2002.

Mechanical properties of native and engineered cartilage from indentation tests

G. Spatafora¹, D. Deponi², A. Pozzi², F. Gervaso³, A. Sannino³, A. Addis⁴, M. Campagnol⁴, G. Peretti⁵, and F. Boschetti^{1,6}

¹ *LaBS (Laboratory of Biological Structure), Dipartimento di Ingegneria Strutturale, Politecnico di Milano, Milan*

² *San Raffaele Scientific Institute, Milan*

³ *Dipartimento Ingegneria dell'Innovazione, Università del Salento,*

⁴ *CRABCC, Rivolta d'Adda (CR)*

⁵ *Department of Sport, Nutrition and Health Sciences, University of Milan*

⁶ *IRCCS Istituto Ortopedico Galeazzi, Milan*

Abstract—Several biomechanical methods are applied to cartilage to characterize and quantify its mechanical properties. In this work, we focused our attention on the evaluation of mechanical characteristics of articular cartilage performing indentation tests on native and engineered pig cartilage. Results showed a significant difference between native and engineered cartilage.

Keywords—Swine articular cartilage, creep tests, microindentation, engineered cartilage.

I. INTRODUCTION

ARTICULAR cartilage is composed of a charged solid matrix phase consisting of charged proteoglycan macromolecules and collagen fibers, an interstitial fluid phase, and an ion phase [1]. The function of articular cartilage is to support and distribute loads in the diarthrodial joints, and to minimize friction between opposing articular surfaces by the maintenance of a lubricating fluid film [2]. Experimental investigation of cartilage biomechanics during compression is typically performed by using confined or unconfined compression, or indentation. The equilibrium response of articular cartilage is satisfactorily described, for small deformations, by the homogeneous isotropic elastic model [3]. In particular, unconfined compression and indentation tests are commonly used to evaluate the Young modulus E , whereas confined compression tests are performed to evaluate the aggregate modulus and the permeability.

In this work we focused our attention on the evaluation of the mechanical characteristics of articular cartilage using indentation tests. The indentation technique has been applied for studies on normal [4], degenerated [5] and repaired [6] articular cartilage. The popularity of this method is due to the relative facility of performing an indentation experiment and the availability of a classical mathematical solution for contacting elastic bodies [7]. Advantages of indentation include the ability to analyze samples *in situ* and the possibility to perform multiple tests at several different sites. Furthermore, if typical confined or unconfined compression tests require excision of cartilage from the subchondral bone, indentation tests allow maintenance of the cartilage-bone interface integrity. Thus, the aim of this work was to evaluate the mechanical properties of swine articular cartilage by micro-indentation. In particular, our tests were performed both on samples of swine articular cartilage, obtained from a

natural and untreated femoral condyle, and on samples of different types of specimens extracted from condyles treated and repaired by an engineered cartilage, in order to evaluate the mechanical behavior of each type of implant and to compare it with the properties of native articular cartilage.

II. MATERIALS AND METHODS

Six adult pigs were used as experimental animals (weight approximately 80 kg). Engineered constructs were implanted on patellar groove in different positions. Three lesions were created in each side of the patellar groove in each pig. The cartilaginous lesions were subjected to three different treatments:

- untreated: the cartilage lesion was free to self-repair;
- cells: a scaffold seeded with articular chondrocytes was implanted in the lesion site;
- no-cells: a cell-free scaffold was implanted.

Implants of engineered cartilage were extracted after 12 weeks. The characteristics of tested samples are resumed in Table 1.

TABLE I
SAMPLES GEOMETRIC CHARACTERISTICS

	# Samples	Thickness [mm] (mean±SD)
<i>Cells</i>	5	3.7924±0.7400
<i>No-Cells</i>	4	3.2704±1.0987
<i>Untreated</i>	4	3.2536±1.9564
<i>Native</i>	9	2.0594±0.5604

The thickness of native cartilage was measured using a stereomicroscope (Nikon SMZ800), equipped with a camera (Nikon DS-5M) using the software NIS-Elements D 2.20; each sample was cut along the transversal direction, after proper re-equilibration time following the indentation tests. The thickness of cartilage implants, instead, was measured by histology.

Indentation tests were performed by an electromagnetic machine (Enduratec ELF 3200, Bose Corporation, ElectroForce Systems Group, MN USA), equipped with a 22N load cell. Indentation creep testing of all the samples was performed using plane-ended indenters with a diameter of 2.0 mm. To maintain hydration, samples were kept in a PBS bath throughout all the tests (Fig.1).

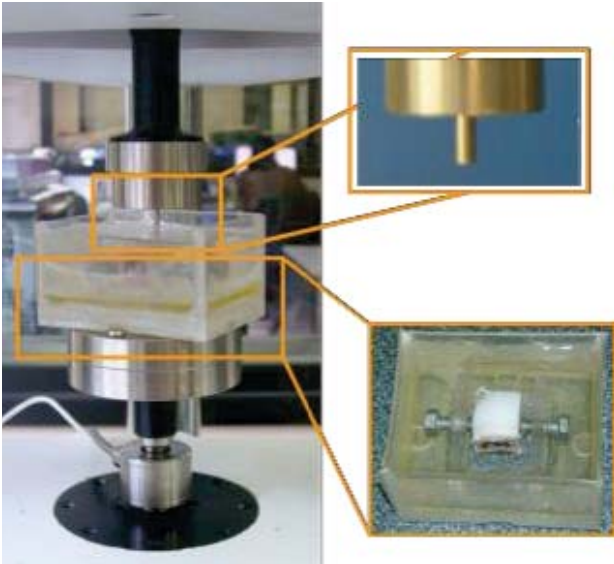


Fig. 1. Particular of experimental setup with a particular of the cylindrical indenter and of the cartilage sample housing.

Both for native and engineered cartilage a pre-load of -0.01N was applied. Each specimen was mechanically tested under creep stepwise micro-indentation tests applying two increasing levels of force (-0.02N and -0.04N) at a compression rate of 0.1N/s for, 1220s and 1620s respectively.

Indenter displacement was finally evaluated. A typical creep response is shown in Figure 2:

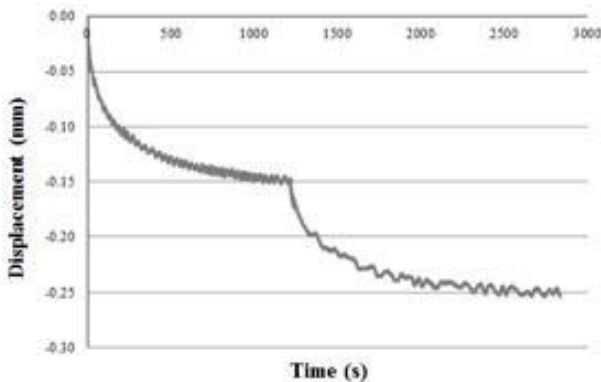


Fig. 2. Typical creep response for one of samples tested by indentation.

Mechanical properties of native and engineering cartilage were evaluated using the mathematical formulation proposed by Hayes et al. [3]. In particular, Hayes' theoretical formulation, models cartilage as a mono-phasic material bonded to a rigid space (bone). Mak et al. [7], models cartilage as a bi-phasic material (solid elastic matrix and a fluid phase). Both mono-phasic and bi-phasic theories give the same mathematical formulation for equilibrium responses (Eq. 1):

$$E = \frac{F(1 - \nu^2)}{2a\omega_0\kappa} \quad (1)$$

Where E is the Young modulus, F is the measured force, ν is the Poisson's coefficient, a is the indenter ratio, ω_0 is the absolute deformation and κ is a theoretical scaling function related to the Poisson's coefficient and the ratio between the indenter radius and the sample thickness (a/h). We used a Poisson's ratio equal to 0.2 [8] and κ values as reported in

[9].

III. RESULTS

Table II resumes the Young moduli obtained from the experimental tests previously described for each engineering stress applied to each group of samples:

TABLE II
VALUES OF YOUNG MODULUS (E)

	$\sigma_1 = -0.008 \text{ MPa}$	$\sigma_2 = -0.016 \text{ MPa}$
<i>Cells (n=5)</i>	0.0164 ± 0.0060	0.1066 ± 0.0392
<i>No-Cells (n=4)</i>	0.0176 ± 0.0087	0.1027 ± 0.0445
<i>Untreated (n=4)</i>	0.0183 ± 0.0075	0.0904 ± 0.0230
<i>Native (n=9)</i>	0.1028 ± 0.0391	0.2878 ± 0.093

We analyzed results using ANOVA tests to understand the differences between the three different types of implants and native cartilage in terms of stiffness. The first ANOVA test ($\alpha=0.5$) was applied to the three types of implants and resulted in no significant difference of each one to the other. We then compared native cartilage to tissue engineered cartilage (the three groups together), in this case the differences were statistically significant.

IV. DISCUSSION AND CONCLUSION

The Young modulus of engineered cartilage samples are significantly lower than those of native cartilage and there is not a significant difference between the three group of engineered tissues. A reasonable explanation is that the implant time was too short for the implanted engineered sample to fully reproduce the complex structure of cartilage tissue.

REFERENCES

- [1] V.C. Mow, S.C. Kwei, W.M. Lai, C.G. Armstrong "The extracellular matrix, interstitial fluid and ions as a mechanical signal transducer in articular cartilage" *Osteoarth. Cartil.*, vol. 7, pp. 41-58, 1999.
- [2] V.C. Mow, L.A. Setton "Mechanical properties of normal and osteoarthritic articular cartilage", in *Osteoarthritis*, K.D. Brandt, m. Doherty and L.S. Lohmander, Oxford University Press, Oxford, UK, 1998, pp 108-122.
- [3] W.C. Hayes, L.M. Keer, G. Herrmann, L.F. Mockros "A mathematical analysis for indentation test of articular cartilage" *J. Biomechanics*, vol. 5, pp 541-551, 1978.
- [4] V.C. Mow, M.H. Holmes, W.M. Lai "Fluid transport and mechanical properties of articular cartilage: a review" *J. Biomechanics* vol. 17, pp 377-394, 1984.
- [5] R.D. Altman, J. Tanenbaum, L. Latta, W. Riskin, L.N. Blanco, D.S. Howell "Biomechanical and biochemical properties of dog cartilage in experimentally induced osteoarthritis" *Ann. Rheum. Diss.* vol.43, pp 83-90., 1984
- [6] R.R. Whipple, M.C. Gibbs, W.M. Lai, V.C. mow, A.F. Mak, C.R. Wirth "Biphase properties of repair cartilage at the articular surface" *Trans. Orthop. Res. Soc.* vol 10, pp 340, 1985.
- [7] A.F. Mak, W.M. Lai, V.C. Mow "Biphase indentation of articular cartilage -I. Theoretical analysis" *J. Biomechanics*, vol. 20, pp 703-714, 1987.
- [8] F. Boschetti, F. Gervaso, G. Pennati, G.M. Peretti, P. Vena, G. Dubini "Poroeleastic numerical modelling of natural and engineered cartilage based on in vitro tests" *Biorheology*, vol. 43, pp 235-247, 2006.
- [9] M. Zhang, Y.P. Zheng, A.F.T. Mak "Estimating the effective Young's modulus of soft tissues from indentation tests - nonlinear finite element analysis of effects of friction and large deformation" *Med Eng Phys* vol. 19, pp 512-517, 1997.

Effects of calibration errors on 3D kinematics quantification with fluoroscopy

L. Tersì¹, S. Fantozzi^{1,3}, L. Cristofolini^{1,2,4}, and R. Stagni^{1,3}

¹ *Health Sciences and Technologies – Interdepartmental Center for Industrial Research (HST – ICIR),*

² *Department of Mechanical, Nuclear, Aviation, and Metallurgical Engineering (DIEM),*

³ *Department of Electronics, Computer Science, and Systems (DEIS), University of Bologna, Bologna, Italy*

⁴ *Medical Technology Lab, Rizzoli Orthopaedic Institute, Bologna, Italy*

Abstract—Model based 3D fluoroscopy can quantify joint kinematics with a mm/deg accuracy level. A calibration based on the acquisition of specific devices is usually applied to size the system. This study aimed at the characterization of the sensitivity of the pose estimation accuracy to errors in the calibration process, in order to evaluate a possible simplification of the calibration procedure. In-silico simulations were performed to analyse a data-set obtained adding controlled perturbation in the calibration process. The estimation of the rotations was scarcely influenced by calibration errors, while a linear trend was highlighted for translations with a sensitivity of 20% correspondent to approximately a 1 mm error for realistic calibration errors. This error is compensated when computing relative kinematics between two joint segments.

Keywords—Human joint kinematics, 3D Fluoroscopy, Calibration, Computer simulation.

I. INTRODUCTION

CLINICAL [1], and methodological [2] applications are based on the accurate knowledge of in-vivo kinematics of intact and replaced joints. 3D fluoroscopy (3DF) is a technique that allows to accurately reconstruct joint kinematics, combining series of 2D X-ray fluoroscopic projections, and the knowledge of 3D geometric models of relevant bony segments or prosthetic components [3]. 3D models can be acquired using intact joints CT or MRI datasets, or prostheses CAD; 2D projections are typically gathered using clinical fluoroscopes and C-arms. Fluoroscopic images, however, are affected by sigmoidal and pincushion distortion, and the accuracy, with which the X-ray focus position is operatively set, is affected by the physical deformation of the C-arm [4] and is dependent by the specific acquisition setup.

To step from qualitative to quantitative analysis, algorithms are applied to properly size a virtual model of the fluoroscope, to correct for image geometrical distortion, and to calibrate the position of the X-ray focus, acquiring known geometry devices such as 2D calibration grid and 3D calibration cage. Kinematics is quantified optimizing an alignment metric that match the 3D model to the relevant fluoroscopic projections.

3DF theoretically permits to achieve a millimetre/degree accuracy level in joint motion analysis [3]). Several sources of error contribute to this accuracy and were previously characterized: local optima of the metric [5], segmentation inaccuracies [6], symmetries of the models [5], geometrical distortions [7]. Conversely, the extent to which X-ray focus calibration affects

the reliability of the measurements has not been clarified yet. Some authors proposed to assume the X-ray focus centered in the image plane and to consider valid the focus distance provided by the fluoroscope [8]. This assumption may be useful to simplify the 3DF setup and analysis, especially for clinical applications, but neglecting the calibration may lead to a further loss of accuracy of the measurements.

The present work is aimed at the in-silico characterization of the calibration, specifically investigating the sensitivity of the accuracy of 3DF to X-ray focus calibration error.

II. MATERIAL & METHODS

1) *Data-set*: The acquisition system was outlined defining a global reference frame with x and y axes parallel, z -axis perpendicular to the image plane, and with the origin in the center of the image plane. The X-ray source was virtually placed in $F_{ref} = (F_x, F_y, F_z) = (0, 0, 1000)mm$ representing a typical distance of a standard fluoroscope, and pixel spacing was fixed at $0.3 mm$, as for typical images. No geometrical distortion was considered as already successfully investigated in a previous study [7].

High resolution models of humerus, ulna, and radius were downloaded from the official site of the European project VAKHUM (contract #IST-1999-10954¹) and used to generate the controlled fluoroscopic dataset. An anatomical reference frame was associated to each bone model according to the ISB recommendations, and the Euler zxy convention was adopted for rotations. Each model was placed in 3 reference random poses $P_{ref} = [T_x, T_y, T_z, \Theta_x, \Theta_y, \Theta_z]_{ref}$ and flat shaded projections were generated.

2) *Pose estimation algorithm*: The implemented alignment algorithm was based on 3D surface models and adaptive distance maps (DM) with a resolution of $0.5 mm$ [5]. The pose was estimated minimizing with a memetic algorithm [9] the euclidean root mean square distance (RMSD) between the surface model and the beam of lines connecting the X-ray source focus and the edge of the bone, extracted in the projected image.

3) *Data analysis*: For each model, the pose $P_{est} = [T_x, T_y, T_z, \Theta_x, \Theta_y, \Theta_z]_{est}$ was estimated considering the perturbed focus position in the following permutations, for a total

¹http://www.ulb.ac.be/project/vakhum/public/_dataset/public-data.htm

TABLE I

SENSITIVITY (S) AS THE SLOPE OF THE LINEAR REGRESSION OF THE ESTIMATION ERROR ΔP OF THE HUMERUS VS THE IMPOSED CALIBRATION UNCERTAINTY ΔF , AND COEFFICIENT OF DETERMINATION (R^2).

DOF	F_x		F_y		F_z	
	S	R^2	S	R^2	S	R^2
T_x [$mm \cdot mm^{-1}$]	0.20	0.90 *	0.00	0.00 *	0.00	0.00 *
T_y [$mm \cdot mm^{-1}$]	0.00	0.00	0.20	0.98 *	0.00	0.00
T_z [$mm \cdot mm^{-1}$]	0.01	0.00	0.05	0.00 *	0.21	0.09 *
Θ_x [$deg \cdot mm^{-1}$]	0.00	0.00	-0.05	0.29 *	0.00	0.00 *
Θ_y [$deg \cdot mm^{-1}$]	0.06	0.88 *	0.00	0.00 *	0.00	0.00 *
Θ_z [$deg \cdot mm^{-1}$]	0.00	0.00	0.00	0.00 *	0.00	0.00

* ANOVA $P < 0.01$

of 375 alignments:

$$F_{per} = F_{ref} + \Delta F, \text{ with } \begin{cases} \Delta F_x = [-5, -1, 0, 1, 5] \\ \Delta F_y = [-5, -1, 0, 1, 5] \\ \Delta F_z = [-10, -2, 0, 2, 10] \end{cases} \quad (1)$$

representing ranges of typical calibration errors, and using the contour extracted from the flat shaded reference images.

The deviation between estimated and reference pose was quantified as $\Delta P = P_{est} - P_{ref}$. The n-way ANOVA ($\alpha = 0.01$) was used to assess significant effects of bone model, reference pose, and focus calibration error on the pose estimation errors. To quantify the entity of the effect, the sensitivity of the estimation of each DOF was determined as the slope ($S = \Delta P / \Delta F$) of the fitting linear regression of data. The coefficient of determination (R^2) was also reported.

III. RESULTS

A statistically significant effect ($P < 0.01$) of the three random reference poses on the estimation error of each DOF was highlighted: the pose with the smaller portion of visible bone in the FOV produced larger errors. ANOVA highlighted also that a significant effect of the bone model: the radius showed a largest bias and dispersion of P_{est} (best case scenario 0 ± 0.2 deg for Θ_z , worst case scenario 6 ± 5 mm for T_z).

The perturbation Δy (y axis nearly parallel with the bone longitudinal axis) had a significant effect on all the DOF estimations, while ΔF_x affected T_x and Θ_y , and ΔF_z influenced T_x , T_z , Θ_x , Θ_y and Θ_z . Notwithstanding these statistically significant differences, only in few cases a correlation trend was found in the data. In particular, any calibration error in one direction is reflected in a concordant error in the estimation of the translation in the same direction, approximately equal to the 20% of the calibration error. The coefficient of determination R^2 is larger than 0.90 for T_x and T_y , but equal to 0.09 for T_z . The rotation around the projection axis Θ_z is not linearly dependent on ΔF but a small correlation is found between Θ_y and ΔF_x and between Θ_x and ΔF_y . Table I resumes the results for the humerus bone model.

IV. DISCUSSION AND CONCLUSIONS

The effect of 3DF calibration error on the pose estimation accuracy was evaluated considering in-silico simulations. A robust memetic algorithm was used for the optimization in order to reduce the effects of metric local minima.

Reference pose, and bone model had affected the results due to the intrinsic symmetries of the reference model and contours. The simulated calibration errors (ΔF) significantly affected the pose estimation. A linear correlation with a sensitivity of approximately 20% was found between the calibration error in one direction and the estimation of the concordant translation. However, the coefficient of determination R^2 was small for T_z due to the intrinsic variability of the estimation of the translation along the projection axis z [5]. A linear correlation was found also between ΔF_x and Θ_y but with low sensitivity (0.06 deg/mm) and thus with a minor impact on the pose estimation accuracy.

Concluding, calibration errors mainly affected the estimation of translations: typical calibration error of 5 mm in x , and y directions, are reflected in a concordant pose estimation error of 1 mm. The effect on the rotations is statistically significant but of low intensity. Calibration errors affect 3DF accuracy, but it might be disregarded when sub-millimetre accuracy is not needed, as for potential clinical application.

ACKNOWLEDGEMENT

This project was supported by the research grant ‘‘A multimodal approach to study the biomechanics of healthy and pathological knee’’ (PRIN 2008).

REFERENCES

- [1] S. Zuffi, A. Leardini, F. Catani, S. Fantozzi, and A. Cappello, ‘‘A model-based method for the reconstruction of total knee replacement kinematics.’’ *Medical Imaging, IEEE Transactions on*, vol. 18, no. 10, pp. 981–991, 1999.
- [2] R. Stagni, S. Fantozzi, and A. Cappello, ‘‘Double calibration vs. global optimisation: Performance and effectiveness for clinical application.’’ *Gait & Posture*, vol. 29, no. 1, pp. 119–122, 2009.
- [3] S. A. Banks and W. A. Hodge, ‘‘Accurate measurement of three-dimensional knee replacement kinematics using single-plane fluoroscopy.’’ *IEEE Transactions on Bio-Medical Engineering*, vol. 43, no. 6, pp. 638–49, Jun. 1996, PMID: 8987268.
- [4] L. P. Nolte, M. A. Slomczykowski, U. Berlemann, M. J. Strauss, R. Hofstetter, D. Schlenzka, T. Laine, and T. Lund, ‘‘A new approach to computer-aided spine surgery: fluoroscopy-based surgical navigation.’’ *European Spine Journal*, vol. 9 Suppl 1, pp. S78–88, Feb. 2000, PMID: 10766062.
- [5] L. Tersi, S. Fantozzi, and R. Stagni, ‘‘3D elbow kinematics with mono-planar fluoroscopy: in-silico evaluation.’’ *EURASIP Journal on Advances in Signal Processing*, vol. 2010, 2010.
- [6] M. R. Mahfouz, W. A. Hoff, R. D. Komistek, and D. A. Dennis, ‘‘Effect of segmentation errors on 3D-to-2D registration of implant models in x-ray images.’’ *Journal of Biomechanics*, vol. 38, no. 2, pp. 229–239, Feb. 2005.
- [7] E. Gronenschild, ‘‘The accuracy and reproducibility of a global method to correct for geometric image distortion in the x-ray imaging chain.’’ *Medical Physics*, vol. 24, no. 12, pp. 1875–1888, 1997.
- [8] M. S. Zihlmann, H. Gerber, A. Stacoff, K. Burckhardt, G. Szekely, and E. Stssi, ‘‘Three-dimensional kinematics and kinetics of total knee arthroplasty during level walking using single plane video-fluoroscopy and force plates: A pilot study.’’ *Gait & Posture*, vol. 24, no. 4, pp. 475–481, Dec. 2006.
- [9] L. Tersi, R. Stagni, S. Fantozzi, and A. Cappello, ‘‘Genetic algorithm as a robust method for the joint kinematics estimation with mono-planar 3D fluoroscopy.’’ Edinburgh, Scotland UK, Jul. 2010.

Development and sensitivity study of a hybrid FE-MB model of the human middle ear

G. Vollandri¹, F. Di Puccio¹ and P. Forte¹

¹ Department of Mechanical, Nuclear and Production Engineering, University of Pisa, Pisa, Italy

Abstract— In the present study a hybrid model of the human middle ear is described: a finite element model of the tympanic membrane was combined with a multibody model of the ossicular chain and related soft tissues (joints, ligaments and muscle tendons), through a feedback control strategy. A calibration procedure based on ascertained published experimental data was used to tune parameters whose values are unspecified or widespread in the literature. The sensitivity of the calibrated models to material, geometrical and inertial parameters of both tympanic membrane and ossicular chain was evaluated.

Keywords — ear mechanics, finite element method, multi-body method, parameter calibration.

I. INTRODUCTION

THE human middle ear (ME) includes the ossicular chain (OC) and the tympanic membrane (TM), which can be considered as either part of the outer or middle ear.

Both lumped (e.g. multi-body (MB)) and distributed (mainly finite element (FE)) parameter modelling approaches have been applied for the simulation and prediction of the ME dynamic behaviour in physiological or pathological conditions, e.g. [1,2]. While the FE method is particularly suitable for the complex geometry and the material orthotropy of the TM, the ossicles can be considered as rigid bodies and a MB approach can be adopted to improve joint representation [3].

In this study, a hybrid FE-MB model was developed, through a feedback control strategy of the complete ME, combining a FE model of the TM with a MB model of the OC and surrounding soft tissues. Some characteristics were taken from recent literature models [2,4,5], however the model was also calibrated by fitting on ascertained published experimental data [6]. The sensitivity of the calibrated model to both TM and OC parameters was finally investigated.

II. ANATOMY OF THE MIDDLE EAR

Located in the ear canal, the TM (Fig. 1) is firmly anchored to the temporal bone, by the tympanic annulus (TA). Two main regions, called “pars tensa” (PT) and “pars flaccida” (PF), are conventionally identified in the TM, both having a complex composite structure [7-9].

The OC is made of three ossicles: malleus, incus and stapes. The malleus has a long portion named manubrium, firmly embedded between the layers of the TM, up to the TM center point (*umbo*) and is connected to the incus through the incudo-malleolar joint (IMJ). The incus articulates with the stapes through the incudo-stapedial joint (ISJ). The stapes includes the stapes footplate (SFP), which is connected to the oval window (OW) of the inner ear.

The OC is supported by ligaments, four inserting on the malleus, one on the incus. An annular ligament joins the periphery of the SFP to the OW. The tendons of two muscles, the tensor tympani and the stapedius, attach to the manubrium and the stapes neck, respectively [7].

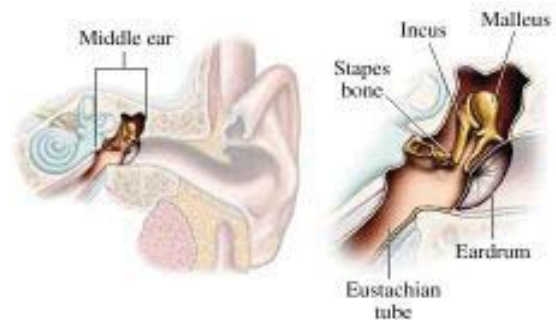


Fig.1. Middle ear schemes (reprinted with permission from <http://hearingaidscentral.com/howtheearworks.asp>).

III. METHODS

A. Tympanic membrane model

An FE model of the human TM was developed in Ansys[®] 11. The geometry of a human TM (with a uniform thickness equal to 74 μm value) was deduced from an anatomic model [10]. Thicknesses and material properties were deduced from [4,5]. A 200 μm thickness value was adopted for the TA. The PT was assumed orthotropic with Young's moduli (E) in the radial and circumferential directions equal to 35 MPa and 20 MPa, respectively. On the contrary the PF was considered isotropic with $E=10$ MPa. Both the TM and the TA were modelled with shell elements. A rigid region was defined, for the insertion of the manubrium of the malleus into the TM.

B. Ossicular chain model

A 3D multibody model was developed in the SimMechanics (*Matlab*[®], *MathWorks*) environment. The model structure includes rigid bodies representing the ossicles and the lumped cochlear load mass; ideal mechanical joints to simulate the synovial IMJ and ISJ and the connections at the ends of the OC (TMMJ and SOWJ); spring and damper elements to represent the linear visco-elastic response of soft tissues, in particular at the connections of the ligaments and tendons to the tympanic cavity and at the TMMJ, IMJ, ISJ and SOWJ.

The location of ossicle centers of mass and inertia tensors were deduced from [2] whereas the mass values from [4]. The widespread range of joint and ligament E values in the literature suggested a calibration procedure. A γ angle [2] was

introduced for defining the anterior-posterior ligament axis.

Two different configurations of the model were calibrated, with moveable or fixed IMJ, due to the controversial assumption on IMJ mobility.

C. Hybrid FE/MB middle ear model

Combining the previously described models of the TM and the OC, a hybrid FE/MB model of the complete ME was developed. A feedback control strategy was adopted, Fig. 2. The eigenvalue results from the FE model were used to develop a state space model of the TM [11]. Through linearization, a state space linear model of the OC was obtained.

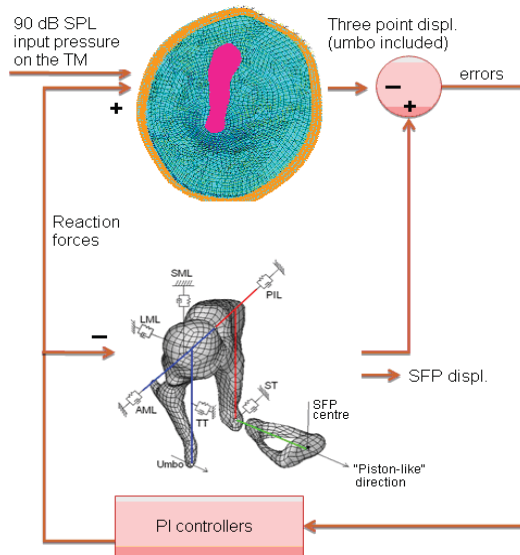


Fig. 2. Scheme of the middle ear model..

A 90 dB sound pressure level sinusoidal pressure input was applied to the TM.

Three error functions (i.e. the difference between the current displacement value and the reference one [6]) are provided as input of three proportional-integral controllers. The experimental values of umbo and SFP displacement amplitude as function of frequency, published in [6], were assumed as reference for the calibration procedure, based on optimization algorithms, in order to identify unspecified parameters but also to tune some parameters whose literature values range over orders of magnitude.

D. Sensitivity analysis

For the sensitivity analysis the 6 DoF IMJ configuration of the calibrated model was preferred.

Concerning the TM model, the selected parameters were the PT, PF and TA thicknesses, E , TM size and cone depth. Concerning the OC model, ossicle masses, γ angle, stiffness and damping constants of ligaments and tendons were varied.

Where available, reference lower and upper boundary values from the literature were adopted. The size and cone depth of the TM were reasonably varied in the $\pm 25\%$ range. Values twice and half the calibrated one were adopted for the CO stiffness and damping coefficients and γ angle..

As index of sensitivity, a percentage relative variation was computed as the ratio of the Root Mean Square (RMS) values of the varied and reference vectors over the analyzed frequency range.

IV. RESULTS AND DISCUSSION

Umbo and SFP displacement amplitudes, fitted on experimental data [6], are presented in Fig. 3 showing how our model fits better than the corresponding FE one. In particular, the 6GdL IMJ configuration proves to be more appropriate in the high frequency range.

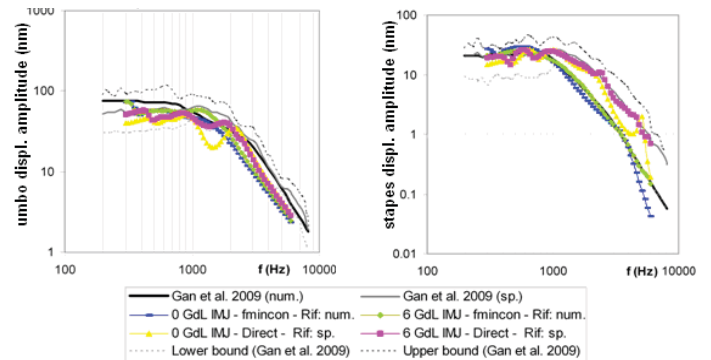


Fig. 3. Umbo (left) and stapes footplate (right) displacement amplitude.

As far as the TM model parameters are concerned, the results, expressed by the umbo/SFP curves, show a higher sensitivity to thickness, and to the increased E . On the other side for the OC model parameters, the results show a higher sensitivity to the γ angle and to the elastic/damping constants. Therefore these parameters must be more accurately estimated by measurements or calibration in order to have a reliable model to reproduce the middle ear performance in physiological conditions and predict performance variations following surgical interventions and prosthetic replacement.

REFERENCES

- [1] F. Zhao, T. Koike, J. Wang, H. Sienz, R. Meredith, "Finite Element Analysis of the Middle Ear Transfer Functions and Related Pathologies", *Med Eng Phys*, vol. 31, pp. 907–916, 2009.
- [2] T. Wright, "The Linear and Nonlinear Biomechanics of the Middle Ear", *University dissertation, Dept. of Otolaryngology, University Hospital, S22185 Lund, Sweden*, 2005
- [3] G. Volandri, F. Di Puccio, P. Forte, S. Manetti, "Model-oriented Review and Multi-Body Simulation of the Ossicular Chain of the Human Middle Ear", *Med Eng Phys*, 2011 (submitted). In press
- [4] R.Z. Gan, B. Feng, Q. Sun, "Three-Dimensional Finite Element Modeling of Human Ear for Sound Transmission", *Ann Biomed Eng*, vol. 32, pp. 847–859, 2004.
- [5] R.Z. Gan, Q. Sun, B. Feng, M.W. Wood, "Acoustic-Structural Coupled Finite Element Analysis for Sound Transmission in Human Ear. Pressure Distributions". *Med Eng Phys*, vol. 28(5), pp.395–404, 2006.
- [6] R. Z. Gan, T. Cheng, C. Dai, F. Yang, M. W. Wood, "Finite Element Modeling of Sound Transmission with Perforations of Tympanic Membrane", *J. Acoust. Soc. Am.* vol. 126, pp. 243–253, 2009.
- [7] S. A Gelfand., 2009, "Essentials of Audiology", Thieme.
- [8] G. Volandri, F. Di Puccio, P. Forte, C. Carmignani, "Biomechanics of the tympanic membrane", *J. Biomech.*, 44(7), pp.1219–1236, 2011.
- [9] G. Volandri, F. Di Puccio, P. Forte, S. Manetti, "Modellazione multi-body dell'orecchio umano", *Proc. AIMETA 2011*, pp. 10, 2011.
- [10] <http://audilab.bmed.mcgill.ca/daren/3Dear>
- [11] M. R. Hatch, *Vibration simulation using Matlab and Ansys*, Chapman and Hall/CRC, 2000.